International Journal of Multiphase Flow 88 (2017) 69–86

Contents lists available at ScienceDirect

International Journal of Multiphase Flow

journal homepage: www.elsevier.com/locate/ijmulflow

Study of the impacts of droplets deposited from the gas core onto a gas-sheared liquid film

Andrey V. Cherdantsev[a,b,c,*], David B. Hann[a], Buddhika N. Hewakandamby[a], Barry J. Azzopardi[a]

[a] University of Nottingham, Nottingham, UK
[b] Kutateladze Institute of Thermophysics, Novosibirsk, Russia
[c] Novosibirsk State University, Novosibirsk, Russia

ARTICLE INFO

Article history:
Available online 1 October 2016

Keywords:
Gas-sheared liquid film
Droplet entrainment
Droplet deposition
Droplet impact
Disturbance waves
Laser-induced fluorescence

ABSTRACT

The results of an experimental study on droplet impactions in the flow of a gas-sheared liquid film are presented. In contrast to most similar studies, the impacting droplets were entrained from film surface by the gas stream. The measurements provide film thickness data, resolved in both longitudinal and transverse coordinates and in time together with the images of droplets above the interface and images of gas bubbles entrapped by liquid film. The parameters of impacting droplets were measured together with the local liquid film thickness. Two main scenarios of droplet-film interaction, based on type of film perturbation, are identified; the parameter identifying which scenario occurs is identified as the angle of impingement. At large angles an asymmetric crater appears on film surface; at shallow angles a long, narrow furrow appears. The most significant difference between the two scenarios is related to possible impact outcome: craters may lead to creation secondary droplets, whereas furrows are accompanied by entrapment of gas bubbles into the liquid film. In addition, occurrence of partial survival of impacting droplet is reported.

1. Introduction

In annular gas-liquid flow, the liquid flows as a thin film along channel walls carried downstream by a high-velocity gas stream in the centre of the channel. The film surface is covered by a complex system of nonlinear waves of different scales and speeds. Disturbance waves are the longest and the highest waves in the wavy structure of liquid film. They travel with high speed and carry the major fraction of liquid. They are separated by the areas of thin residual layer often referred to as the base film which is covered by slow ripples. The disturbance waves are covered with fast ripples (Alekseenko et al. 2008). Both fast and slow ripples are generated at the rear slopes of the disturbance waves. Fast ripples can be disrupted by strong gas shear into droplets, which are then entrained into the gas core. Visualisation of ripples break-up events leading to entrainment was reported in a number of papers, the earliest of which was Woodmansee and Hanratty (1969) who employed a horizontal rectangular cross-section channel with liquid flowing along the bottom. Azzopardi (1983) identified two main types of break-up events in vertical pipes: bag break-up and ligament break-up. These were recently confirmed by Pham et al. (2014), who used a rod bundle geometry, and Cherdantsev et al. (2014), utilizing a horizontal rectangular cross-section channel; in the latter case, the break-up types were related to the three-dimensional shape and layout of the fast ripples. Entrainment of liquid leads to increase of pressure drop and heat and mass transfer in the flow; it makes the film thinner and increases risk of dryout in heated ducts. Data on the rate of entrainment (or, more often, fraction of liquid travelling as droplets) was measured in a large number of papers. This fraction grows with both gas and liquid flow rates and can be close to unity (Pan and Hanratty, 2002; Sawant et al., 2008; Cioncolini and Thome, 2010).

Entrained droplets are accelerated by the gas drag force. Their longitudinal velocity may reach the values of the maximum gas velocity in the flow as reported by Fore and Dukler (1995), Azzopardi and Teixeira (1994) and Azzopardi and Zaidi (1998). They also have transverse velocity component (normal to the film surface), due to initial momentum gained by the droplet in process of entrainment, due to turbulent pulsations in the gas phase or due to action of gravity in case of non-vertical flow. Transverse velocity of droplets in various configurations of annular flow was measured by James et al. (1980), Azzopardi (1987) and Badie (2000). It was shown that initial transverse velocity of droplets may reach

* Corresponding author: 1, Lavrentiev ave., Novosibirsk 630090, Russia.
E-mail address: cherdantsev@itp.nsc.ru (A.V. Cherdantsev).

http://dx.doi.org/10.1016/j.ijmultiphaseflow.2016.09.015

up to 2 m/s. James et al. (1980) analysed the effect of turbulent pulsations in the gas phase on droplets movement. They have found that only small droplets (with diameter smaller than 150–250 μm) are susceptible to the action of pulsations and move chaotically, whilst larger droplets follow ballistic trajectories.

Because of the transverse velocity component the droplets eventually reach the film surface and are deposited onto it. Deposition counteracts entrainment, transferring mass back from the entrained fraction to the liquid film. It is widely accepted that at large distance from the inlet, the rates of entrainment and deposition become equal and flow becomes stabilized. As a rule, deposition rate has been measured as an integral quantity either by double extraction of liquid film (e.g., Cousins and Hewitt 1968; Sawant et al. 2008) or by measuring concentration of tracer liquids (Leman et al. 1985; Pitton et al. 2014).

As well as the integral influence on the mass balance, the droplet impacts may affect the flow properties in a mechanical way. Film surface perturbation due to the impact may increase local roughness of film surface. There can be local thinning of the film at the bottom of a crater caused by impact, which increases probability of dry spot formation. Droplet impact may cause secondary entrainment which leads to change in droplets size distributions.

Most experimental studies of droplet impact on liquid surface involve artificially created droplets. A very large number of such papers were devoted to normal impact of a droplet onto static film, starting from Worthington (1877) to modern experimental and theoretical investigations (Thorrodsen et al. 2008; Van Hinsberg et al. 2010; Bisighini et al. 2010; Lagubeau et al. 2012, etc.). The same technique as the one used in the present paper was recently applied to study normal droplet impact onto static film by Hann et al. (2016). Entrapment of gas into liquid by normally impacting droplets was reported by Oguz and Prosperetti (1990), Thoroddsen et al. (2003).

In annular flow, the droplets are expected to hit liquid surface obliquely and the film surface is covered by waves of different length, amplitude, velocity, slope and curvature. Thus, this situation is rather different from that of normal impact onto static film; instead, oblique impact onto moving wavy film should be investigated to experimentally simulate the impacts of "natural" droplets in annular flow. Besides, the droplets will probably be rather fast and small.

Oblique impacts onto static surface of deep liquid layer were studied experimentally by Leneweit et al. (2005) and Okawa et al. (2008). The work by Leneweit et al. was focused on patterns of spreading of droplet material over liquid surface, depending on impingement angle and droplet Weber number. Liquid perturbation was found to be elongated in the direction of the impact; change of its length and instantaneous velocity of its growth were measured. The results of Leneweit et al. were reproduced well in the model of Watanabe et al. (2008). The work of Okawa et al. (2008) was focused on the effect of the angle between droplet trajectory and liquid surface on creation of secondary droplets. It was found that for large angles asymmetric craters are formed on liquid surface and the rims of the craters may be broken into the droplets. For the angles below 20° secondary entrainment never occurs; liquid perturbation looks rather like a patch of "highly agitated" surface than like a crater. An impact number based on absolute velocity of impacting droplet was shown to be a satisfactory criterion for occurrence of secondary droplets.

Another way to study oblique impact is to drop a droplet vertically onto inclined liquid film was used by Zhao et al. (2011) and Che et al. (2015). In addition to change of the angle between the droplet and the surface (70° and 45° respectively), this approach produces thinner wavy films which makes the situation closer to the case of annular flow. In both papers, it was the transition between coalescence and splash phenomena that was the focus of the investigation. Finally, in the papers by Samenfink et al. (1999) and Alghoul et al. (2011) impact of artificially introduced droplets onto horizontal gas-sheared liquid film was studied. Alghoul et al. (2011) introduced droplets vertically, but, due to the gas flow, the droplets were deformed and they gained small longitudinal velocity component. In this paper the focus was also on transition to splash. Samenfink et al. (1999) fired in droplets at different angles and studied the effect of the angle of impingement on the properties of secondary droplets created due to the impact.

The results obtained in model experiments might be extrapolated onto the case of real annular flow; however, experimental validation of such extrapolation is necessary. Besides, not all the conditions describing the impacts of droplets in annular flow (very fast and small droplets at very shallow angles) were reproduced in existing model experiments. Moreover, reproducing certain aspects of impacts in real annular flow (such as impact of droplets onto disturbance waves) is hardly reproducible in any model experiments. Thus, experimental study of droplet impacts in annular flow is required.

Only a few papers have reported on studies of the impacts of naturally entrained droplets in annular flow. Cousins and Hewitt (1968) performed visualisation of impacts of droplets in upward annular flow onto thin residual layer of liquid remaining on the pipe walls after primary extraction of liquid film. It was found that the impacting droplets created longitudinally oriented "streaks" on film surface. Pham et al. (2014) performed backlit visualisation of gas-sheared liquid film on the outer surface of a cylinder - part of a rod bundle. They presented a number of impact events with formation of a liquid ligament and creation of secondary droplets. Alekseenko et al. (2014a) investigated droplet impacts in downward annular flow using LIF-technique in one longitudinal section of the pipe. They have measured maximum depth and width of the craters, created by impacting droplets, together with spreading velocities and typical lifetime in a wide range of experimental conditions.

Annular flow is a well known challenge for both experimental and theoretical studies. Interaction between the phases results in a large number of complex hydrodynamic processes of various spatial and temporal scale, which are strongly interrelated to each other. This includes generation, evolution and interaction of disturbance waves and ripples, entrainment and deposition of droplets, entrapment of gas bubbles, etc. Creation and validation of physically based models of annular flow requires detailed experimental information on all these processes.

The goal of this paper is to present systematic investigation of the impacts of droplets depositing from the gas core onto the wavy gas-sheared film. The measurements are to be resolved in both longitudinal and transverse coordinates with sufficient spatial and temporal resolution. Brightness-based laser-induced fluorescence (BBLIF) technique will be used to study droplets and liquid film simultaneously to determine the effects of the parameters of the impacting droplet and local properties of liquid film on film perturbation due to impact and on the impact outcomes.

2. Experimental setup and measurements technique

Experimental setup and measurements technique in the present work are essentially the same as those used by Alghoul et al. (2011) and Cherdantsev et al. (2014). Only a brief description of the setup and technique will be given here; for more details the reader is referred to those other papers. The working section of the rig is a horizontal rectangular duct (Fig. 1) manufactured from acrylic resin. The duct is of 161 mm width, 25 mm height and 2000 mm length. Air and water were employed as the

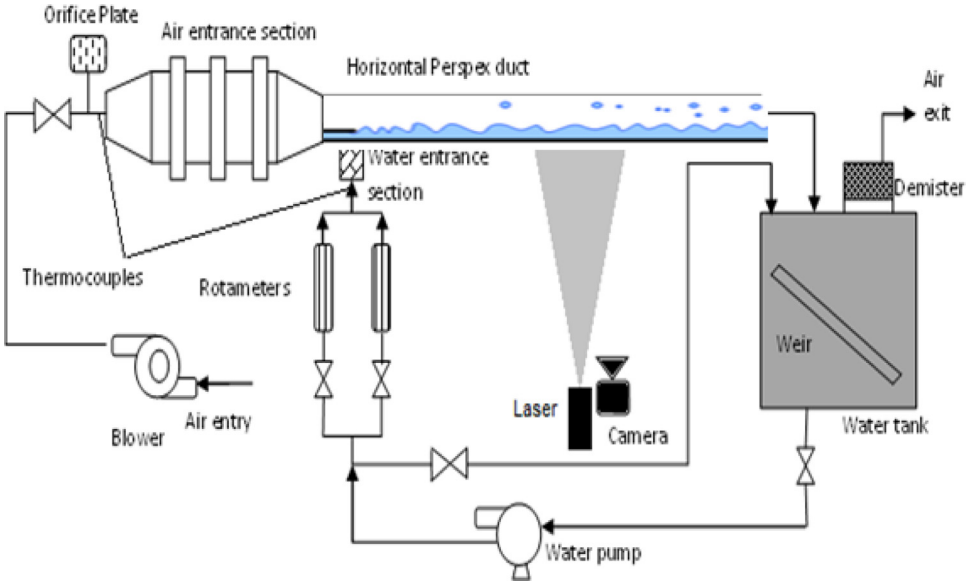

Fig. 1. Scheme of the flow facility.

working fluids. Water was introduced onto the bottom of the duct as a film via a tangential slot.

The measurements were performed at the distance of 1600 mm (37 duct hydraulic diameters) from the inlet. The brightness-based laser-induced fluorescence (BBLIF) technique was used to study the impact events. Fluorescent dye (Rhodamine 6 G) is dissolved in the liquid at a small concentration (15 mg/l). To excite fluorescence, the liquid is illuminated by a pulsed ND: YLF laser with wavelength of 527 nm. The pulse rate and duration were 10 kHz and 100 ns, respectively. The laser beam was expanded over a rectangular area of the bottom of the duct. Local brightness of reemitted fluorescent light was measured with a *Phantom* high-speed camera synchronised with the laser pulse at frame rate of 10 kHz. The camera was used with an orange low-pass filter to block the exciting laser light. Local thickness of liquid layer, h, can be extracted from the measured brightness values using a Lambert-Beer law. For details of the method of conversion from brightness to film thickness, see Cherdantsev et al. (2014). The error of film thickness measurements for the base film region and the rear slopes of disturbance waves can be estimated as 5–6% (see Alekseenko et al. 2014b). At the steep slopes of the interface local overestimation of film thickness is possible due to total internal reflection of the laser light. Such situation generally occurs at the front slopes of the fast ripples and at the edges of bubbles entrapped by liquid film.

The only significant difference from the experiments of Cherdantsev et al. (2014) is the size of the region of interrogation. The earlier work was aimed at obtaining an overall picture of the interfacial structure. Here, a smaller region was studied to obtain more details (51 mm longitudinally and 20 mm transversely). Thus, spatial resolution was improved to 40 μm per pixel, enabling us to resolve much smaller bubbles and droplets. Flow rates corresponding to gas superficial velocities, V_g, of 25, 30 and 35 m/s and liquid Reynolds numbers, Re_L, of 220, 360 and 520 were selected for the study as there was more drop deposition activity. V_g was defined as volumetric gas flow rate divided by cross-section area of the duct, and Re_L was defined as the volumetric liquid flow rate per unit width of the duct divided by the kinematic viscosity of liquid. For each combination of flow rates three records with duration of 0.2 s each were obtained.

Fig. 2 shows a graphic representation of an example of the instantaneous distribution of measured film thickness, h, over the area of interrogation. Longitudinal and transverse coordinates are denoted in this Figure as x and y, respectively. Vertical coordinate is denoted as z. Brightness of each pixel of such an image is directly proportional to the local film thickness measured at this point. White corresponds to film thickness values of 2 mm and higher. Thinner (darker) region of the base film covered by slow ripple waves is present in the left and the right edges of the image. The middle part is occupied by a disturbance wave, which is covered by fast ripples.

The droplets are seen in such images as bright circles or ellipsoids moving faster than the waves. Fluorescent matter contained in droplet liquid also contributes to the measured film thickness. Despite the fact that the droplets are detectable is extremely important for our investigations, there are important considerations. Firstly, local film thickness under an entrained droplet is overestimated by the technique. Secondly, the size of the droplet in z direction cannot be obtained directly from LIF data; not only because of presence of the film, but also due to possible focusing of the exciting light if the droplet is ellipsoidal (see the Appendix 1 in Alekseenko et al. 2014a). So, the size of the droplet can be measured only in x-y plane. Third, the distance between the film surface and the droplet is unknown. It means that the z-coordinate of the droplet and, consequently, z-component of the velocity of the droplet cannot be measured in the present configuration of the measurements technique.

Entrapped air bubbles are visible as bright rings with dark centres. The bright rings appear due to total internal reflection of the exciting light at the borders of the bubbles. The centres are dark since the bubble itself does not contain fluorescent matter. The bubbles are useful for the present investigation, because of their strong links to the droplet impact processes. Local concentration and dynamics of the bubbles will be reported in a separate paper. Supplementary video 1 shows the temporal evolution of film, droplets and bubbles together for the same flow conditions as shown in Fig. 2 during 40 ms period.

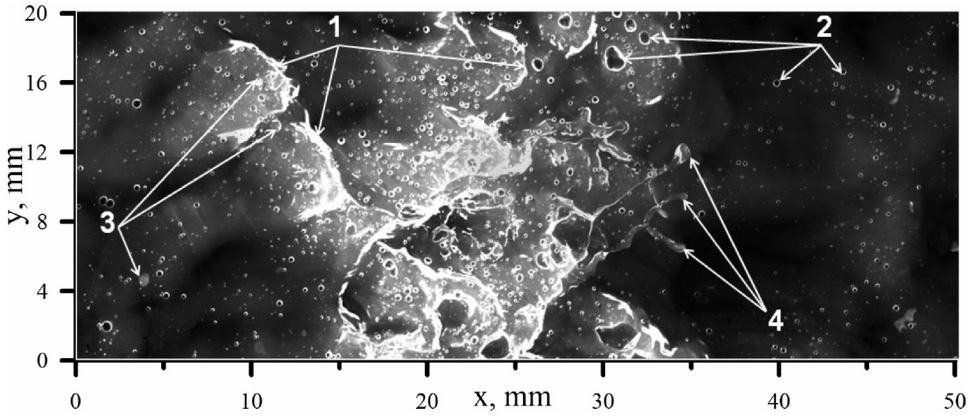

Fig. 2. Example of instantaneous distribution of film thickness over the whole region of interrogation. The numbers denote: fast ripples (1); air bubbles (2); liquid droplets (3); liquid bag broken into jets prior to entrainment (4). $Re_L = 360$, $V_g = 35$ m/s.

3. Results

3.1. Impact detection and classification

To obtain quantitative data all the impact events were detected and processed. The detection process is much more complex compared to studying impacts of artificially introduced droplets, since the impacts of naturally entrained droplets may occur in any point of the Region of Interest (*RoI*) and at any moment of time. Automatic procedure of impacts detection is technically possible, but it is complicated and risky because of high probability of errors. The errors are related to existence of the many other objects of similar temporal and spatial scale in LIF data. In particular, there are: bubbles entrapped by the film; other droplets flying above liquid surface; optical distortions under the steep fronts of the fast ripples. These objects are likely to either produce false impacts detectable by an automatic algorithm or to prevent the algorithm from detecting real impacts. For this reason, visual search for the impact events with manual detection of the impact coordinates in space and time was performed.

For each impact, the event time, t_0, and coordinates, x_0 and y_0, of the initial contact of droplet and film was recorded. For this, an auxiliary procedure in Matlab was written. This procedure allowed us to scroll the frames forward/backward in time, watching them on a large display and marking each impact event with a mouse click. Accuracy of detection of impact coordinates was within 2–3 pixels of the raw image. The program also put a sign on the marked impact so that the same impact event would not be processed more than once; it also allowed us to cancel marking if the impact event was marked by mistake or just not precisely enough; returning back in time to double-check for missed events was also possible.

At the present frame rate and exposure time the captured sequential frames show a highly discrete sequence of instantaneous positions of the droplet and stages of film and droplet perturbation. This means that, if the droplet velocity is large enough, neighbouring frames might show the droplet far from the impact point and already formed crater or furrow in the next frame. For that reason the frame at which film perturbation was first observed was considered to be the time of the first contact and coordinates of the first contact were defined based on film perturbation shape. Namely, the centre of the first appearance of the crater and the beginning of a furrow were recorded as impact coordinates (definitions of craters and furrows are given below).

All the observed film perturbations due to droplet impact were recorded, except for two cases: (i) the impacts occurring at the very border of *RoI* were ignored since much information about the impact is lost beyond the borders of *RoI* in this case; (ii) impacts of the remnants of transitional entrainment structures – liquid bags and ligaments – onto the base film in front of disturbance waves were not recorded. Only the impacts caused by droplets which have already detached and formed into spherical or ellipsoidal shape, were processed. After the processing, over 3600 impact events were recorded for all the 54,000 frames. The relative frequencies of the impacts (given in number of impacts per square centimetre per second) are shown in Fig. 3.

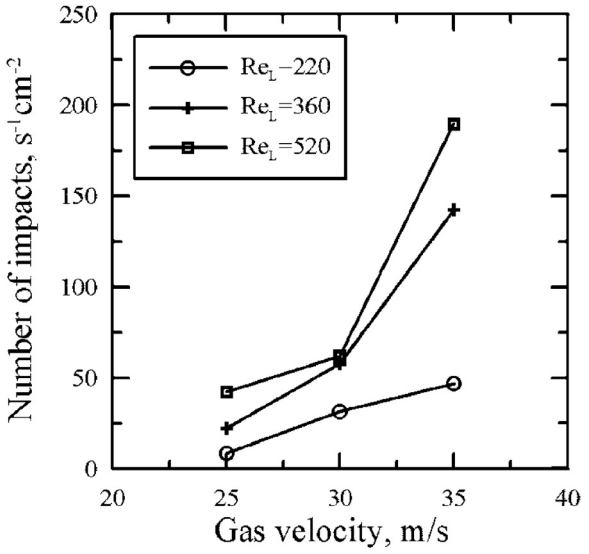

Fig. 3. Number of impacts per unit area (cm^2) per second.

The frequency of the impacts increases strongly with increase of either gas or liquid flow rates. This is not surprising, since the number of impacts obviously depends on the number of entrained droplets (e.g., Azzopardi 1997), and the fraction of liquid entrained increases with both gas and liquid flow rates. It might seem strange that increase in gas velocity by 40% (from 25 to 35 m/s) leads to increase in the number of impact by 400–600%. On the other hand, the droplets start to be entrained in such a system from a critical value of superficial gas velocity, V_c, estimated to be in the range 16 to 20 m/s (see Fig. 12 in Cherdantsev et al. 2014). If V_c is subtracted from each gas superficial velocity, the ratio of the two gas velocities is then between 200–300%.

The increase in entrained fraction of liquid is not the only reason of increasing the number of impacts. During the detection process, it was observed that the local number of impacts in-

creases greatly when disturbance waves appear. The first increase occurs in front of a disturbance wave when significant portion of new-created droplets deposit promptly onto the base film just in front of the disturbance wave. The second increase occurs at the rear slope of a disturbance wave, which collects large number of droplets that would have impacted the film much farther downstream if there was no disturbance wave there.

A visual inspection of impact events was performed to classify the impacts. It was found that two main types of surface perturbations may occur due to droplet impacts. The first type results in a crater being formed at the interface, which is similar to what is observed during normal droplet impact onto static liquid surface. An example of crater evolution is shown in Fig. 4. As in Fig. 2 and similar subsequent Figures, local brightness is proportional to local film thickness. In Fig. 4 the frames are given with time step, T, equal 0.5 ms, which means that every fifth frame is shown. Different values of T will be used for subsequent Figures of the same sort. For similar Figures below, diameter, d, and velocity in horizontal plane, V_{xy}, of the impacting droplets will be specified in the Figure caption. For the method of measurements of these two parameters see the next subsection.

Due to asymmetry of the impact, the rim of the crater is typically asymmetric as well, being much higher at the leeward side of the crater. Break-up of the rim into jets and then into droplets only occurs on the leeward side. If there is no rim, the perturbation of film surface is approximately symmetric. The full evolution of this event can be seen in the Supplementary video 2.

In the second type of impact a droplet creates a long and narrow furrow on film surface (see Fig. 5). The droplet quickly protrudes from the point of initial contact with the film over a finite distance, leaving behind a highly perturbed surface. This surface is covered by transverse "wrinkles" with very small wavelength. Such a complete event is shown in Supplementary video 3. These perturbations are similar to those observed by Cousins and Hewitt (1968) caused by deposition of droplets on the surface of thin residual film created after the removal of the original film. In contrast to the crater case, numerous bubbles are entrapped by the film surface over the whole length of the furrow. To the best of the capabilities of the present measuring system, nearly no secondary droplets are created due to furrow impact.

These observations correlate with those made by Okawa et al. (2008), who studied oblique impacts of droplets onto static liquid surface. They also noted the asymmetric form of the crater and its crown in case when the angle between droplet trajectory and liquid surface was over 20°s. When the angle was smaller than 20°s, they observed that droplets created long patches of highly agitated film surface. Though they did not report anything about the bubbles creation, the latter case, presented by Okawa et al. (2008) in their Fig. 1d looks very similar to the creation of furrows reported in the present work.

It is supposed that these similarities are true in our case: when the angle between the droplet trajectory and the film surface is relatively large, a crater, with possible asymmetric rim, appears; when the angle is smaller than some critical value (not necessarily equal to that found by Okawa et al.), a furrow is created.

In these experiments, the film surface just before impact is not always horizontal. Hence, the angle of impingement, γ, is actually a sum of two angles: the angle between droplet trajectory and horizon, α, and the slope of film surface prior to impact, β (see Fig. 6). In the present configuration of the BBLIF technique we cannot measure the distance between the droplet and the film surface. This means that we cannot measure the vertical component of the droplet's velocity, V_z, and, hence, the angle α. On the other hand, the angle β can be measured directly and it can be used to estimate the critical value of γ from below (see Section 3.2).

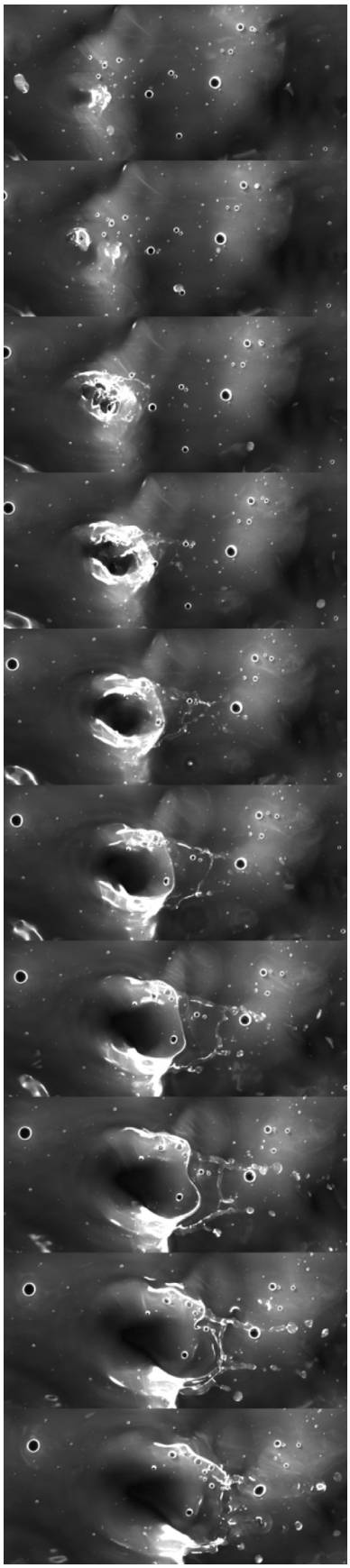

Fig. 4. Example of droplet impact creating a crater causing secondary entrainment of droplets. $V_g = 25$ m/s, $Re_L = 360$, $T = 0.5$ ms; size of the images is 22*10 mm. $d = 1.09$ mm, $V_{xy} = 9$ m/s.

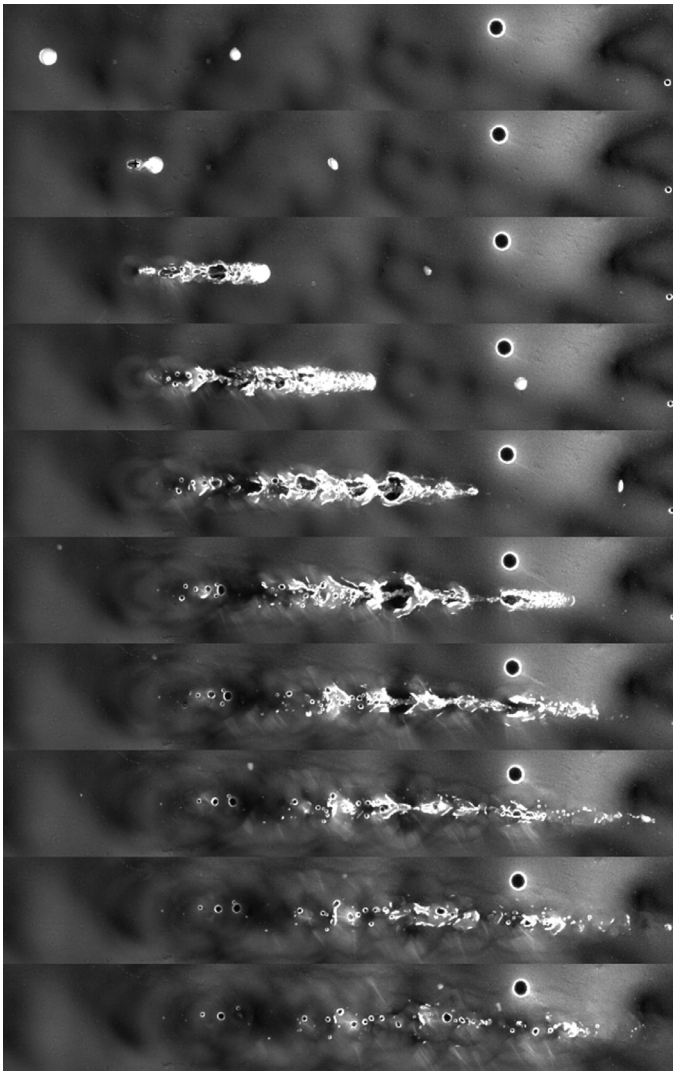

Fig. 5. Example of droplet impact creating a furrow causing entrapment of bubbles. $V_g = 25$ m/s, $Re_L = 220$. $T = 0.2$ ms; size of the images is 28*4 mm. $d = 0.71$ mm, $V_{xy} = 20$ m/s.

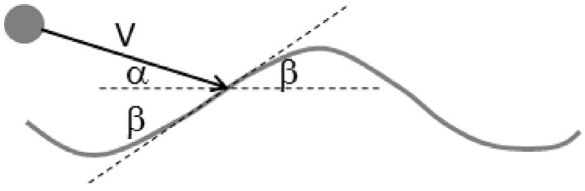

Fig. 6. Sketch showing the impact angles.

A third type of event is survival of the impacting droplet (Fig. 7). An example of such an occurrence is shown in Supplementary video 4. At the initial point of contact, either crater or furrow – the latter is rarer – is created. The top part of the droplet does not sink into the film; it continues to travel with the same velocity while the bottom part has already stuck to the film. The middle part of the droplet is stretched and finally ruptured (see Section 3.5 for more details), releasing the upper part to continue its flight. Most likely, this kind of event occurs when a droplet with large horizontal and small vertical velocity components hits the crest of a ripple. In the present classification the survival events were separated from 'normal' craters or furrows, since in this case part of the droplet momentum does not contribute to the film perturbation.

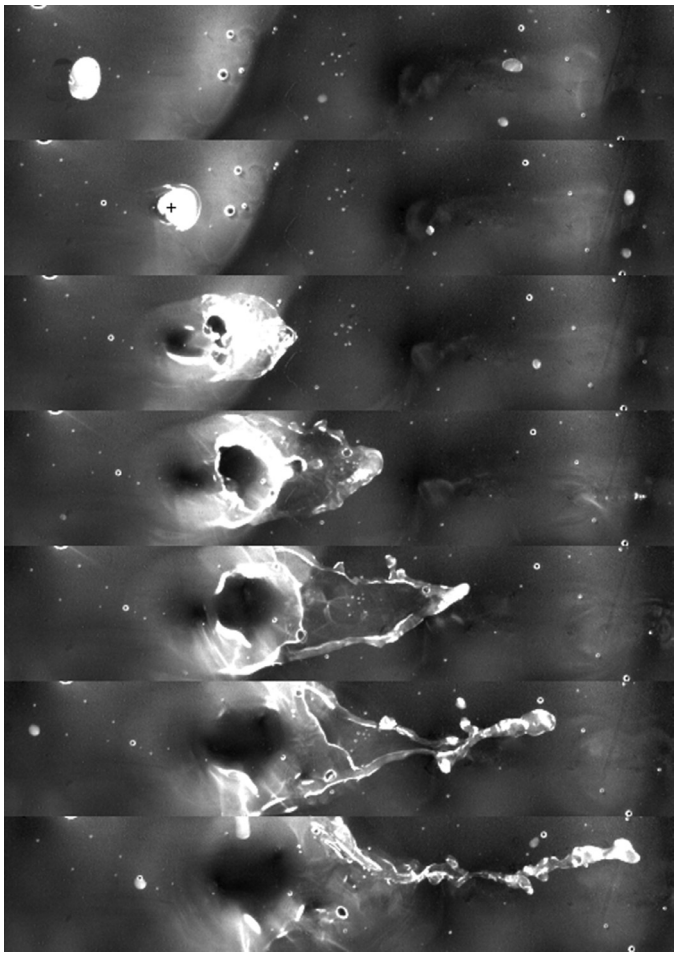

Fig. 7. Example of droplet impact with survival of the initial droplet. $V_g = 30$ m/s, $Re_L = 220$. $T = 0.4$ ms; size of the images is 22*6.5 mm. $d = 1.23$ mm, $V_{xy} = 7.09$ m/s.

Fig. 8 shows the relative frequencies of the impact types for all flow conditions. The frequencies are approximately the same and do not show any distinct trend with either gas or liquid flow rate. Furrows appear more often than the others, representing about 55–60% of events, craters make 30–35% and the relative frequency of survival events is only ~5%.

3.2. Measurements of the impact parameters

To quantify the various impact types, it is necessary to know those parameters which define the impact. This includes properties of film and droplet prior to impact. As a rule, in the further processing the impact events for all gas and liquid flow rates will be analysed together. This approach is based on two main premises:

(1) The impact is defined by the properties of the impacting droplet and liquid film;
(2) Scatter of properties of both film and droplet within one pair of flow rates is much larger than the average effect of flow rates on droplets and local film properties.

The film measurements are relatively simple and automatic, based on the 3D matrix of film thickness, $h(x,y,t)$, obtained by BBLIF method. Three quantities were extracted from this processing for each impact: local average film thickness at the impact point, h_0; local slope of film surface at the impact point, β; local curvature of film surface at the impact point, h_c. For an impact

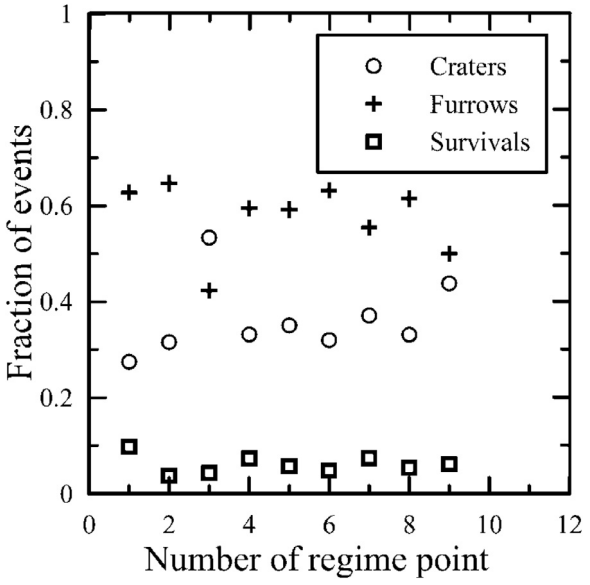

Fig. 8. Relative frequencies of various types of impact events. Each value along abscissa axis corresponds to a certain combination of flow conditions. $V_g = 25$ m/s (1–3); $V_g = 30$ m/s (4–6); $V_g = 35$ m/s (7–9). $Re_L = 220$ (1,4,7); $Re_L = 360$ (2,5,8); $Re_L = 520$ (3,6,9).

Table 1
Maximum absolute error of measurements of film properties prior to impact for given percentage of impact events.

Percentage of impact events	δh_0, mm	$\sigma\beta$, degrees	σh_c, mm^{-1}
40	0.014	0	0.014
60	0.024	0.24	0.034
80	0.04	0.95	0.094
90	0.057	2.15	0.194
95	0.078	4.53	0.298

event with parameters t_0, x_0, y_0, film surface was studied at a time t_0-0.2 ms in order to prevent taking into account the local peak in brightness caused by the presence of the impacting droplet. Short fragment of a longitudinal section of *RoI* at fixed y_0, namely, *h(x0-dx: x0 + dx,y0,t0-0.2 ms)* was selected for processing. For the measurements of h_0 and β, dx was equal 3 pixels or 0.12 mm; for estimation of h_c, dx was equal 25 pixels or 1 mm. Prior to measurements, matrix *h(x,y)* was smoothed with 2D median filter with window size of 50*50 pixels (2*2 mm) in order to minimize the influence of local perturbations of the record caused by bubbles, droplets or optical distortions. h_0 was defined as the average value of the processed fragment; β was defined as arctangent of the coefficient of the highest power in the linear interpolation of the processed fragment. Local film curvature, h_c, was defined in this study as the coefficient of the highest power in parabolic interpolation of the fragment.

In order to characterise reliability of the measurements of h_0, β and h_c, root-mean-square error of every single approximation, namely, σh_0, $\sigma\beta$ and σh_c, was recorded. Then cumulative distributions of these errors were analysed to estimate the maximum value of error of interpolation for certain percentage of impact events. The errors of approximation were then transformed into absolute errors of measurements of β and h_c as:

$$\delta\beta = arctan(\sigma\beta/2dx); \qquad \delta h_c = 2\sigma h_c/dx^2.$$

Here $\delta\beta$ and δh_c are absolute errors of β and h_c measurements, respectively (note that dx was different for determination $\delta\beta$ and δh_c). The error data are summarised in Table 1 for different percentage of impact events.

For the majority of impact events errors of measurements of h_0 and β are small enough (note that the standard deviation of h_0 measurements includes physical slope of the interface and the real error is expected to be smaller). The error is larger for h_c measurements, which is most likely caused by large length over which the interpolation was performed and higher probability of encountering optical distortions, bubbles, etc. However, the main goal of measuring the curvature of the waves at the point of impact was to identify whether the impact occurs at the crest of a ripple or at the trough between the ripples. For this purpose, the sign of curvature is sufficient.

The distributions of impact events by these three parameters are given in Fig. 9 separately for each type of the impact for the whole investigated range of flow conditions.

It can be seen from Fig. 9a that the majority of furrows and survival cases occur when the film is thin, i.e. on the base film between the disturbance waves. Crater impact events are distributed in a much wider range of h_0 values; the main part of these events takes place on disturbance waves (i.e., for h_0 above approximately 0.5 mm).

Fig. 9b shows the distributions by the film slope prior to impact. All the furrow and survival events belong to the range of slopes between −5° to 10°, whilst crater events are distributed in a wide range of values. This is in agreement with the aforementioned idea on the influence of the impingement angle on the impact type. It is reasonable to assume that the angle α (see Fig. 6) is positive for the impacting droplets, and hence the impingement angle $\gamma \geq \beta$. Okawa et al. (2008) suggested that the critical impingement angle is equal 20°. Thus, significant portion of crater events belongs to the range of $\gamma \geq 20°$, whilst the whole range of β for furrows is below the critical value by 10–25°. This is also consistent with the data shown in Fig. 9a, since the slow ripples on the base film are less steep than the disturbance waves and the fast ripples on top of disturbance waves.

The curvature data are shown in Fig. 9c. The majority of the impacts occur on surfaces with negative curvature, i.e., crests of fast or slow ripples. This is more probable than the impact into a trough between the ripples. The fast ripples over which the crater events occur have larger negative curvature than the slow ripples. It is interesting to note that the survival events take place at slightly larger negative curvature than the furrows, which is consistent to the explanation of the survival of droplets proposed above.

Fig. 9d shows comparison of film thickness distribution at the impact points, h_0, to the total distribution of film thickness, h, in form of cumulative distributions. Though the base film thickness occupies about 80% of all the measured values of film thickness, only 50% of impacts occur there. This means that relative frequency of the impacts on the disturbance waves is about 4 times higher than that on the base film. Thus, as it was mentioned above, the disturbance waves are "catching" lots of droplets.

Measurements of the parameters of the impacting droplets are more difficult, because of large velocity and small size of the droplets. Combined with relatively low (for this purpose) camera frequency it makes the procedure of tracking the impacting droplets back in time complicated and risky. Nonzero transverse velocity component of the droplets and presence of bubbles, other droplets and optical distortions enhances the difficulties.

Therefore, measurements of droplets properties were performed semi-manually. First, each droplet was tracked back in time starting from t_0-0.1 ms. Its coordinates were recorded in up to 4 time steps. The coordinates identified were used to measure longitudinal and transverse velocity components, V_x and V_y, of a single droplet by linear approximation of $x(t)$ and $y(t)$ data. The absolute velocity of impacting droplet in a horizontal plane, V_{xy}, can be cal-

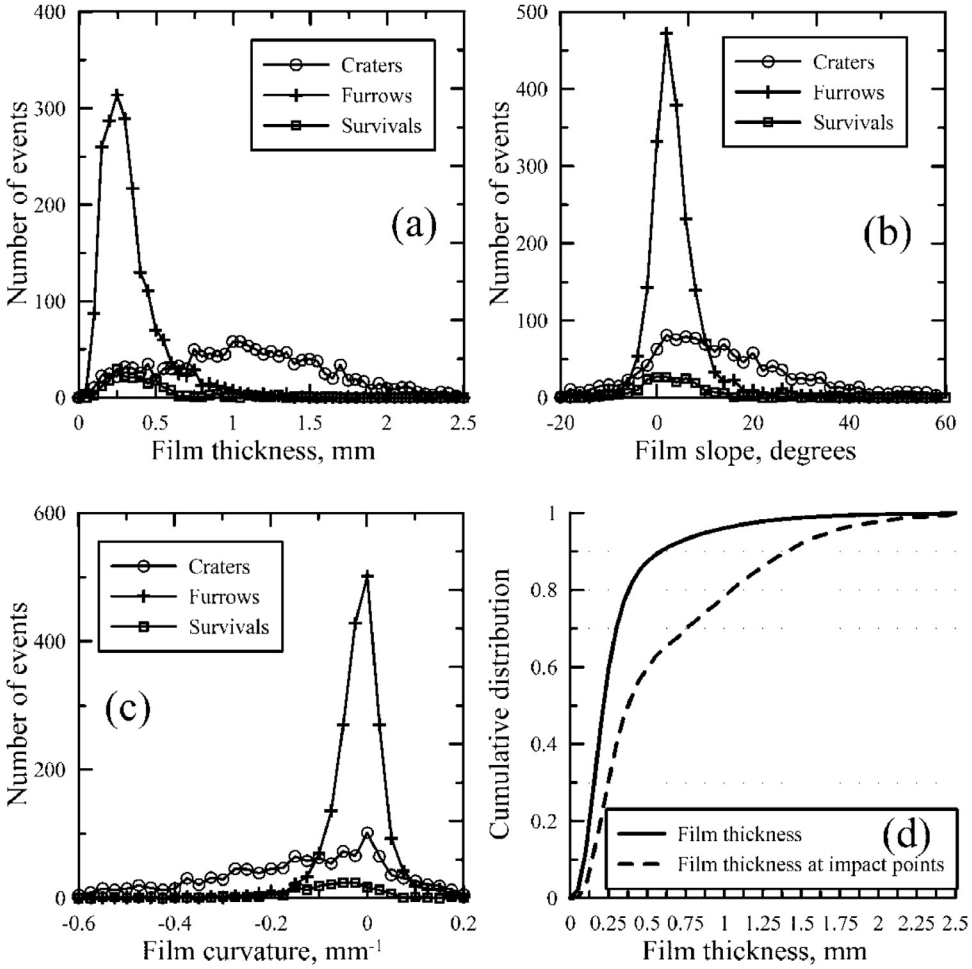

Fig. 9. Distributions of all the impact events by film thickness (a), slope (b) and curvature (c) prior to impact. Separate distributions for craters (1), furrows (2) and survival events (3) are compared. Comparison of cumulative distributions of film thickness and film thickness at impact points (d).

culated as:

$$V_{xy} = \sqrt{V_x^2 + V_y^2}.$$

Measurements of the sizes of droplets were performed for those droplets whose coordinates were successfully identified for several frames. LIF-image of a droplet is actually a sum of brightness emitted by fluorescent matter contained in the droplet itself and in the liquid film under the droplet. Two ways of separation of droplets from the film were used. In the first method, a threshold of 15 μm was used for binarisation of the matrix

$$D(x, y) = h(x, y) - M(x, y),$$

where *M(x,y)* is obtained by applying median filter with filtering window 2*2 mm to *h(x,y)*. This method was expected to work in case of relatively small droplets. The other method was based on assumption that the film surface does not change much over a short time, whilst the position of droplet changes significantly. Thus, frame difference matrix

$$FD(x, y, t) = |h(x, y, t) - h(x, y, t - 0.1\ \text{ms})|$$

was binarised with the same threshold. For the largest and the slowest droplets it is possible that the previous and current image of the droplet will overlap, causing errors. To obtain information in this case, the FD matrix was defined as

$$FD(x, y, t) = |h(x, y, t) - h(x, y, t - 0.5\ \text{ms})|$$

was used. For each detected position of a droplet, all three methods were applied and up to 4 images from 12 images available were selected manually to fit two criteria: they should not contain obvious errors in the identification of the droplet border and they should be the most persistent with respect to time and method of processing. Then for the selected images, average values of the projection area S_{xy} (number of pixels belonging to the droplet) of each droplet were recorded. Equivalent diameter of each droplet was defined using the projection area as if the droplet was circular. Ellipticity of droplets was neglected.

For some of the droplets, identification failed. A number of explanations can be proposed:

(1) Some droplets overlapped with bubbles / other droplets / optical distortions which made the droplet hardly distinguishable;
(2) Droplets with size less than the pixel size ($d < 0.04$ mm) are unlikely to be visible in the present data;
(3) Small droplets are more susceptible to the turbulent pulsations in the gas phase, so they can move chaotically and thus be untraceable.

James et al. (1980) estimated the minimum size of traceable droplets as 0.15 mm; we have observed a number of traceable droplets with $d = 0.12$ mm, but the number of droplets with diameter about 0.08 mm is already very small (see Fig. 11a below). Thus, explanation (3) is expected to be valid. Besides, it includes the droplets mentioned in the explanation (2). Explanation (1) is also more likely to work for smaller droplets.

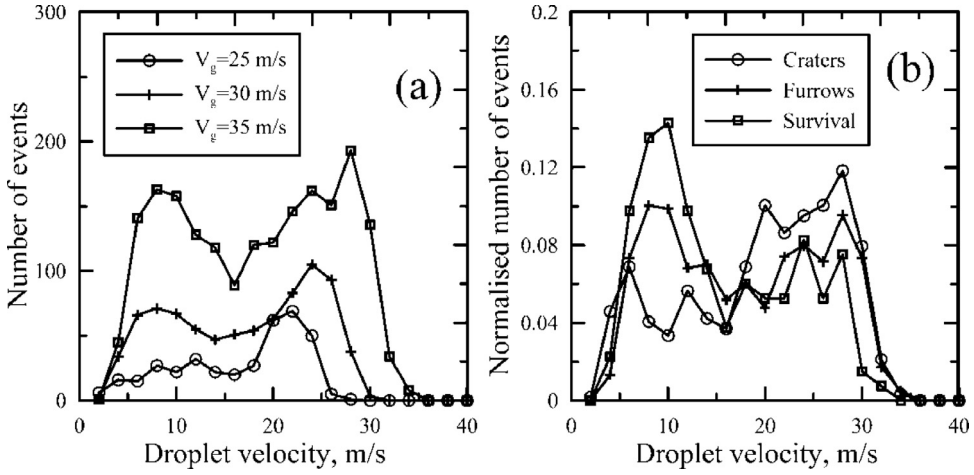

Fig. 10. Distributions of impacting droplets by velocity. (a) All types of impact events for three different gas velocities; (b) Normalized distributions separately for droplets creating craters, furrows and survival events for $V_g = 35$ m/s.

In total, slightly less than 500 droplets (~14% of total number of processed impact events) were not identified. Over 87% of these missed droplets created craters and in 84% cases no secondary droplets were observed (see Section 3.4 for details).

Accuracy of measurements of velocities and diameters of impacting droplets may be estimated as follows. In case of velocities the error is defined by ratio of uncertainty of identification of droplet centres to the distance between the centres of the droplet's images in neighbouring frames. Upper estimate of the numerator is equal to droplet diameter; lower estimate of the denominator is equal to velocity value multiplied by 0.1 (delay between the frames in ms) which gives the distance in mm. Median value of such estimation gives 15% error, which increases for the largest and the slowest droplets. However, in real experiments this error is several times smaller for two reasons. First, the centre of a droplet could be identified much more precisely, and real error in numerator could be estimated as 2–3 pixels or 0.1 mm. Second, for the majority of the droplets, 4 consecutive time frames were processed together, giving three non-independent measurements. This makes denominator three times larger. The error calculated this way makes 1% for the fastest droplets with $V_{xy} = 35$ m/s; 2% for $V_{xy} = 15$ m/s and maximum of 15% for the slowest droplets with $V_{xy} = 2$ m/s. Absolute error is roughly constant (~0.3 m/s) for different velocities of the droplets.

Numerous sources of error of measurements of droplet diameter using BBLIF method were analysed by Alekseenko et al. (2014a). These authors used *RoI* consisting of only one line of pixels oriented longitudinally with spatial resolution of 0.2 mm/pixel, sampling frequency of 50 kHz and exposure of time 2 μs. They analysed:

- error of discretisation, which was random but rather large (up to 10%) of their resolution;
- error of misalignment, when non-central part of a droplet appeared in their *RoI*, leading to systematic underestimation of droplet size by 20–25%;
- error caused by refraction of exciting laser light on curvilinear surface of spherical and elliptical droplets, which was shown to be negligible;
- error of blurring of droplet images due to the finite exposure time, which was shown to be negligible;
- error caused by refraction of fluorescent light on ripples, leading to systematic overestimation by 5–10% for the range of gas velocities used in the present experiments.

In the present experiments, the discretisation error was significantly smaller because the spatial resolution is 5 times better and also due to three-dimensional measurements. The latter still gave us a discrete number of possible droplet diameters, but the step between the neighbouring discrete values decreased with droplet diameter. E.g., for $d = 0.2$ mm this step was about 5 μm or 2.5%. Other source of random error was due to wrong results of automatic separation between the droplets and the film. This error was not completely eliminated, but it was minimised by the visual control procedure described above.

The misalignment error is essentially irrelevant for the present 3D-measurements. Considerations on negligibility of error caused by the refraction on droplets are still valid for the present measurements. Exposure time was 20 times smaller in the present experiments. Error due to refraction on ripples remains significant, though it is expected to be lower in the present case since we were dealing only with impacting droplets, which are, as a rule, very close to the interface.

To summarise, we expect that random error of droplet diameter measurements does not exceed 10% for the droplets of $d = 0.2$ mm and is much lower for larger droplets. Besides, systematic overestimation of droplet diameter by 5–10% is possible due to refraction on ripples with negative curvature.

Fig. 10(a) shows distributions of impacting droplets by V_{xy} for different gas velocities (bin width is 2 m/s). The data on different liquid flow rates are united in these distributions. The velocities of droplets are distributed in a wide range starting from the velocity 2–3 times larger than that of disturbance waves (1–2 m/s) and up to the superficial gas velocities. Though the sample size is not very large, an observation can be made that distributions tend to have two peaks: one at the lowest and one at the largest velocity values. The first peak is related to large number of droplets falling back on film surface soon after being entrained due to initial downward velocity component; such droplets do not live long enough to be accelerated by the gas drag force. The second peak is related to the upper velocity limitation: all the droplets that managed to live long enough to reach maximum velocity are 'gathered' here.

Fig. 10(b) shows the velocity distributions for droplets, creating impacts of different types, for one gas velocity value of 35 m/s. Each distribution is normalized by the total number of impacts of this type. All the three types are distributed in a wide range of velocities and it is difficult to pick out any significant influence of V_{xy} on impact type. It could only be said that at the lowest V_{xy} creation of craters is more probable; this is reasonable since with low V_{xy} the angle α will be larger at the same V_z component.

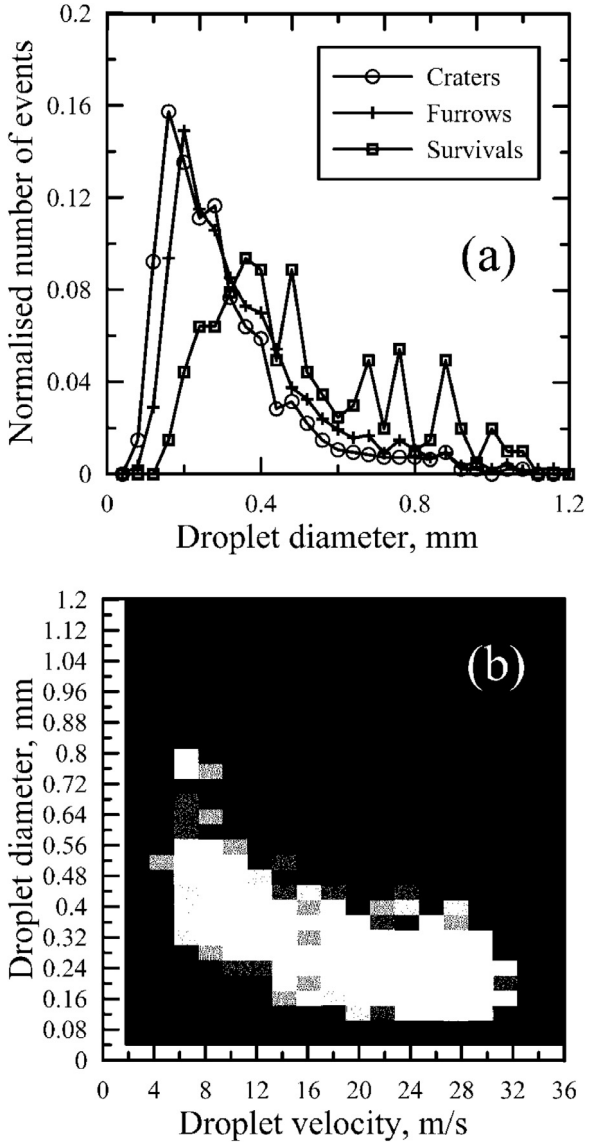

Fig. 11. (a) Normalised distributions of all impacting droplets by diameter for the whole sample. (b) Distribution of impacting droplets by both diameter and velocity, $V_g = 35$ m/s.

The distributions of all the impacting droplets by diameter is shown in Fig. 11(a), separately for furrows, craters and survivals. Bin width is 40 µm. It can be seen that the main amount of droplets belongs to the range of diameters between 0.1 and 1 mm; occasional droplets with size up to 2 mm were observed, but their frequency of appearance is very small. Size distributions of droplets creating craters and furrows are of similar shape, though the distribution of the 'craters' is slightly shifted towards smaller droplets. If we take into account that for over 400 droplets creating craters the size was not measured and that these droplets are expected to have small size, the difference between the 'craters' and 'furrows' distributions is expected to be much stronger. This is quite reasonable since the droplet should be large enough to conserve some amount of liquid beyond the point of initial contact and to be deformed during the furrowing process. The surviving droplets are also characterised by relatively large size. The explanation is the same in this case: the droplet should be large enough to undergo deformation and splitting into two parts.

Fig. 11(b) shows graphical representation of the simultaneous distribution of all the droplets at $V_g = 35$ m/s by diameter and velocity. This number of events in each 2D-bin is given in logarithmic scale; white colour corresponds to the maximum observed number of droplets in the whole distribution (equal 45), whereas black corresponds to absence of droplets in the bin. In general, velocity of the droplets decreases with diameter, since larger droplets need more time to be accelerated by the drag force. Probability of encountering large-diameter droplets with high velocity is low, since they require much time to be accelerated to large values of velocity.

3.3. Furrows and bubbles entrapment

When a droplet creates a furrow, the furrow grows in length with velocity close to that of the droplet. After a short time the protrusion of furrow ceases and the decay of surface perturbations and elimination of portion of the entrapped bubbles is observed.

During the first part of furrow growth stage the impacting droplet is still distinguishable; closer to the end of the growth stage is disappears. The surface beneath the protruding droplet is highly perturbed. It is covered with small-wavelength 'wrinkles' oriented orthogonally to the droplet's trajectory and curving at the edges. Fig. 12 shows examples of the wrinkles for different velocities of the droplets. In the model of Watanabe et al. (2008) it was supposed that these wrinkles appear due to creation of several vortex rings around the impacting droplet. Temporal resolution of the present experiments is not high enough to study inception and evolution of these wrinkles and check if the model interpretation is correct. We can only state that the wavelength of the wrinkles decreases with the velocity of the droplet. This seems reasonable since destabilising effect of larger shear stress induced by a faster droplet should be compensated by stronger surface tension force, hence, smaller radius of curvature of the wrinkles. Thus, it is also possible that the wrinkles appear due to Kelvin-Helmholtz instability induced by the shear induced by the droplet.

The maximum width of a furrow occurs in the middle and it gradually decreases towards the beginning and the end of a furrow. It is obvious that interaction between the liquid droplets and liquid film is very complex, and its complete understanding requires complicated modelling. However, it is possible to perform preliminary experimental analysis of furrow creation using strong simplifications. Two "extreme" simplifications could be made: 1) droplet acts as a solid body, gradually embedding into the film; 2) film acts as a solid wall, and the droplet is spread over its surface. In both cases the shape of the furrow would be the same as it is in the experiments: the local width of the furrow behaves in accordance with the projection area of the droplet in horizontal plane. The bottom and top of the droplet, interacting to the film surface in the beginning and in the end of furrow, respectively, are narrower than the middle part.

In order to characterize the shape of furrows, the main three parameters of each furrow were measured. The length of each furrow, L_f, was defined as the distance between the point of primary contact and the end of the furrow. This quantity was measured in x-y plane. Time of the furrow growth, t_{fg}, was defined as time required for a furrow to reach the maximum length. To measure the average width of perturbed area, W_f, area of furrow existence was processed as follows. Auxiliary matrix $F(x,y)$ was created as:

$$F(x,y) = \frac{1}{t_{fg} - t_0} \left| \sum_{t=t_0}^{t_{fg}} (h(x,y,t) - M(x,y,t)) \right|$$

Here $M(x,y,t)$ is the result of application of 2D median filter to $h(x,y,t)$ with window 2*2 mm. The area occupied by furrow was then identified by finding the values of $F(x,y)$ larger than threshold value proportional to the median value of $F(x,y)$. Then W_f was estimated as the average width of this area over its length.

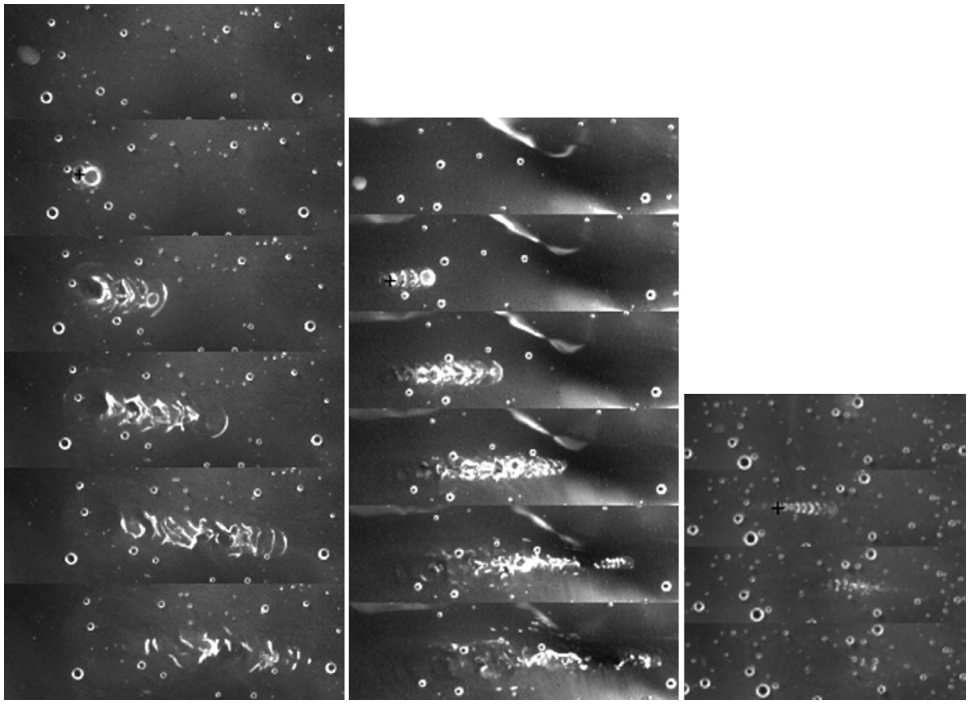

Fig. 12. Examples of furrows. (a) $V_g = 25$ m/s, $Re_L = 520$. $T = 0.2$ ms; size of the images is 9*3 mm. $d = 0.61$ mm, $V_{xy} = 8.3$ m/s. (b) $V_g = 35$ m/s, $Re_L = 220$. $T = 0.1$ ms; size of the images is 8*2 mm. $d = 0.43$ mm, $V_{xy} = 16.7$ m/s. (c) $V_g = 35$ m/s, $Re_L = 520$. $T = 0.1$ ms; size of the images is 7*1.6 mm. $d = 0.28$ mm, $V_{xy} = 23.8$ m/s.

The definition of L_f and W_f are illustrated in Fig. 13. For the example given in this Figure, $t_{fg} = 0.3$ ms. This figure also illustrates the simple idea used for subsequent analysis. Both simplifications mentioned above - assumption of either gradual embedding of the droplet into the film or gradual spreading of the droplet over film surface - imply that the length of a furrow is defined by the droplet's diameter and the impingement angle γ; namely, L_f is expected to be equal $d/tan(\gamma)$. Though γ is unknown, it can be estimated from the dependence of $L_f(d)$. Such dependence is shown in Fig. 14(a) as the average length of furrows, $<L_f>$, for all the droplets belonging to a narrow range of diameters together with its standard deviation, $\pm\delta L_f$. Indeed, $\langle L_f \rangle$ linearly grows with droplet diameter, and the slope of this line corresponds to $\gamma = 6°$ Linear approximations of $<L_f> \pm \delta L_f$ yield estimation that for the majority of furrows γ belongs to range between 4° and 12° These values are quite consistent to the measurements of angle β for furrows (see Fig. 9b).

Fig. 14(b) shows that the length of furrows decreases with droplet velocity in *xy*-plane. On the other hand, Fig. 11(b) shows similar behaviour of droplet diameter on droplet velocity. Thus it can be suggested that the influence of droplet velocity on L_f is actually defined by the influence of droplet diameter on droplet velocity.

The width of furrows created by droplets of different diameter is plotted in Fig. 14(c). Its slope is close to unity (line $W_f = d$ is shown by the dashed line), but it lies about 0.35 mm higher. Thus, there is a minimum width of a furrow even for the smallest droplets. Further increase in the furrow width is related to the increase in droplet diameter. The overall dependence can be described as $<W_f> = d + c$, where c is a constant equal 0.35 mm. It should be also noticed that the standard deviation of W_f does not change significantly with increasing droplet diameter, in contrast to that of L_f.

The most interesting feature of furrows is their ability to create bubbles within the liquid film. According to our observations, this is probably the most important (and, possibly, the only) scenario of bubbles entrapment. To the best of our knowledge, this scenario in annular flow was not previously discussed in literature. Cousins and Hewitt (1968) did not mention bubbles entrapment when they described appearance of furrows due to droplet impact; however, inspection of photographs presented in that work shows presence of bubbles inside the furrows. The number of bubbles in those pictures is smaller than that in our case, which can be explained by thinner film in Cousins and Hewitt (1968) experiments.

In the present state of the experiment it is impossible to conclude how exactly the bubbles are entrapped during furrow impact. The bubbles might appear due to air being physically trapped between the droplet liquid and film liquid while the former is spread over the latter. Otherwise, bubbles might appear in process of collapse of the wrinkles appearing during the furrow growth.

To study this mechanism, an algorithm of automatic detection of bubbles was developed. As shown by Akhmetbekov et al. (2010), the use of the fluorescent imaging technique makes these bubbles easier to identify and discriminate from droplets compared to standard imaging techniques, due to their darker interior and bright ring. Each image was segmented into low and high frequency component using the median of the image taken over a 50×50 pixels square. This estimated the mean film height as the median and identified the high frequency components associated with the bubbles, droplets and other features and the difference between the original and the median image.

The high frequency image of the bubble contained a depression surrounded by a brighter ring. Unfortunately, this is only true for bubbles larger than double spatial resolution (i.e., about 80 μm), so smaller bubbles are ignored in this analysis. The images were quantised to limit the effect of noise and then a watershed analysis was used to detect the depressions associated with bubbles. For each of these watershed regions, the equivalent diameter and centroid was recorded. Regions with eccentricity larger than 2 or over 1000 pixels in size (corresponding to equivalent diameter over 1.4 mm) were filtered out as being associated with the space be-

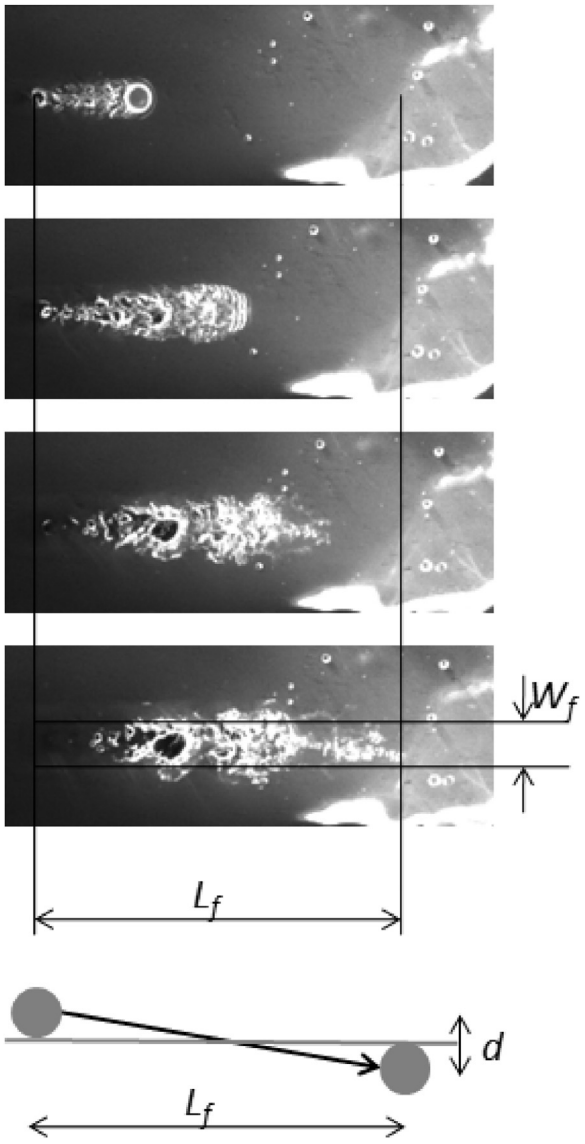

Fig. 13. Definition of the main parameters of a furrow.

tween bubbles or optical distortions. This clearly identified most of the bubbles larger than 2 pixels in size.

In the present work, the algorithm was applied to the areas of existence of furrows; temporal evolution behaviour of number and size of bubbles within this area was studied.

Fig. 15a shows number of bubbles within the area of furrow existence ($L_f{}^*2W_f$) for three long (each with $t_{fg} = 0.9$ ms) furrows. Number of bubbles that existed in this area prior to impact was subtracted from $N(t)$. It can be seen that the new bubbles appear when the furrow grows; after this, some bubbles disappear. The time moment at which the maximum number of bubbles is observed roughly corresponds to the time of furrow growth, t_{fg} (Fig. 15b). Approximation curves in Fig. 15(a) were created in the form:

$$N_{bub} = \frac{2N_0 t_{fg} t}{t^2 + t_{fg}^2}$$

where N_0 is the maximum number of bubbles within this approximation. It is most likely that the bubbles collapse due to relaxation of strong shear induced by the furrowing droplet. A portion of the bubbles survive in this process.

To study the effect of droplets properties on bubbles entrapment, number of entrapped bubbles was normalized over the area occupied by a furrow. This area was taken as $2W_fL_f$ and it is expected to grow as d^2 (see Figs. 14(a,c)). Fig. 16 shows that this normalised number of bubbles does not show any distinct dependence neither on droplet diameter (a) nor on droplet velocity (b). Maximum density of bubbles created by an average furrow is of order 0.9 bubbles per square millimetre; it gradually decreases with time to the value of about 0.15 at $3t_{fg}$. Absolute number of bubbles created by a furrowing droplet is then defined by the area occupied by furrow.

3.4. Craters and secondary entrainment

Secondary droplets are produced when the rim at the leeward side of the crater is broken into jets. The number of jets increases with the size of the crater. For example, the rather large crater shown in Fig. 4 is broken into three jets. Secondary entrainment increases the number of droplets in the gas core and decreases the average size of the droplets, since in this case one large droplet disappears and a number of smaller droplets are created from both film and droplet material. However, the detailed analysis has shown that in the majority of cases of crater impacts (86% in the present experiment) no secondary droplets detectable by the present measuring system were observed.

Example of a crater impact without secondary entrainment is shown in Fig. 17 (compare to Fig. 4). Quite often (as shown in Fig. 17a) even a crater is not formed; only a circular capillary wave is created around the point of contact. In the other cases, the crater appears (Fig. 17 b-c), but its rim is not broken into droplets. The impacting droplets are hardly detectable at these images because of their small size and high velocity.

Okawa et al. (2008) used impact number K as a criterion of secondary droplets creation. This parameter is constructed as function of droplet Weber number, We, and Ohnesorge number, Oh:

$$K = WeOh^{-0.4};\ We = \frac{\rho d V_d^2}{\sigma};\ Oh = \frac{\mu}{\sqrt{\rho d \sigma}}.$$

Here ρ is liquid density, σ - surface tension, μ - dynamic viscosity.

Okawa et al. used the critical value of $K = 2100$ as limit for creation of secondary droplets. Absolute velocity of a droplet in x-z plane was used as V_d. It was shown that this value fits better than that based on vertical velocity component, V_z.

To test this approach, the K number was determined for 764 crater impacts without secondary droplets and 164 crater impacts with secondary droplets. Fig. 18a shows the distribution of 'crater' impacts by K number based on the horizontal velocity of droplet, V_{xy}. Only 16% of droplets impacting without secondary droplets belong to the range of $K \leq 2100$ and for the rest of cases K was much larger, reaching values of 30,000 (Fig. 18(a)). Thus, K based on horizontal velocity does not work as criterion for secondary entrainment. Moreover, the distributions by horizontal velocity are nearly identical for both presence and absence of secondary droplets (Fig. 18b). On the contrary, certain difference exists between the distributions by droplet diameter (Fig. 18c). Taking into account that for 437 impacts without secondary droplets the droplet size and velocity were not measured quite likely due to small size of such droplets (see Section 3.2), the difference is expected to be much stronger.

Absolute velocity used by Okawa et al. is obviously expressed as:

$$V = \sqrt{V_{xy}^2 + V_z^2}.$$

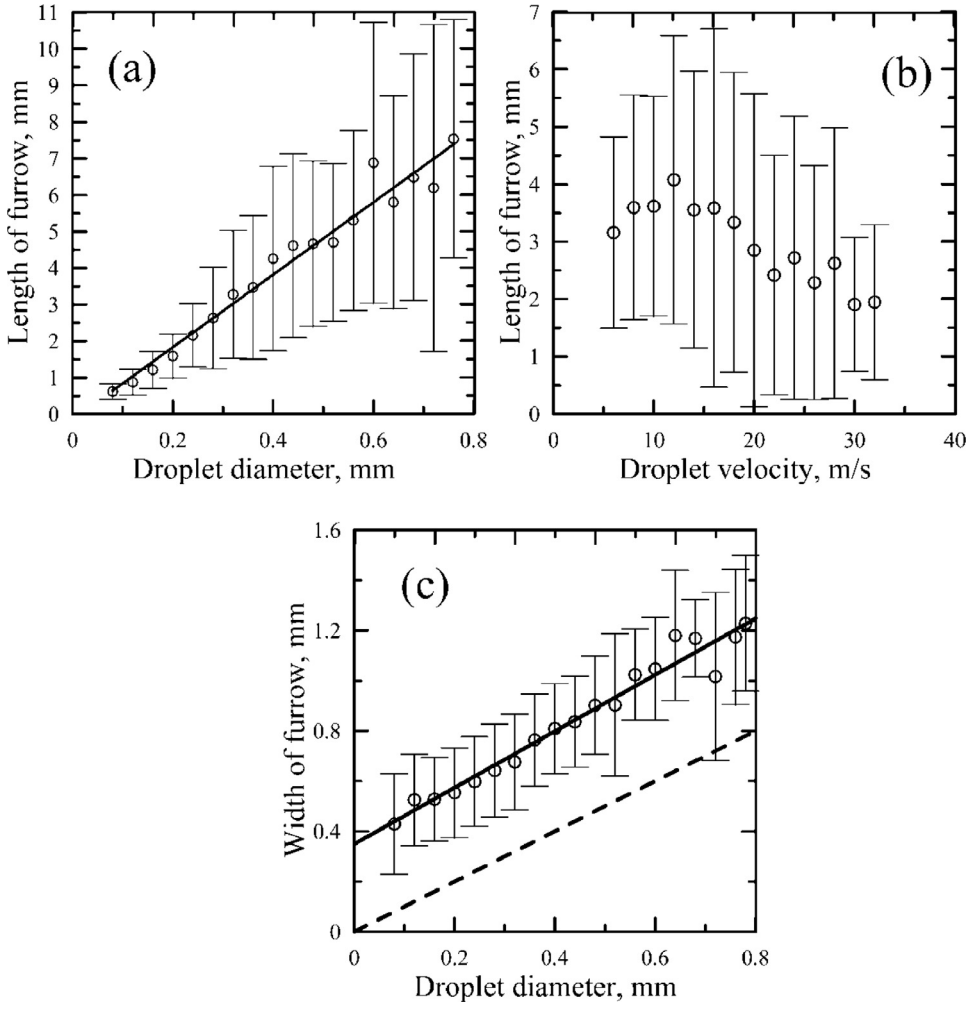

Fig. 14. Average value and standard deviation of length of furrows, created by droplets from narrow range of diameter (a) and velocity (b). (c) Dependence of furrow width on droplet diameter.

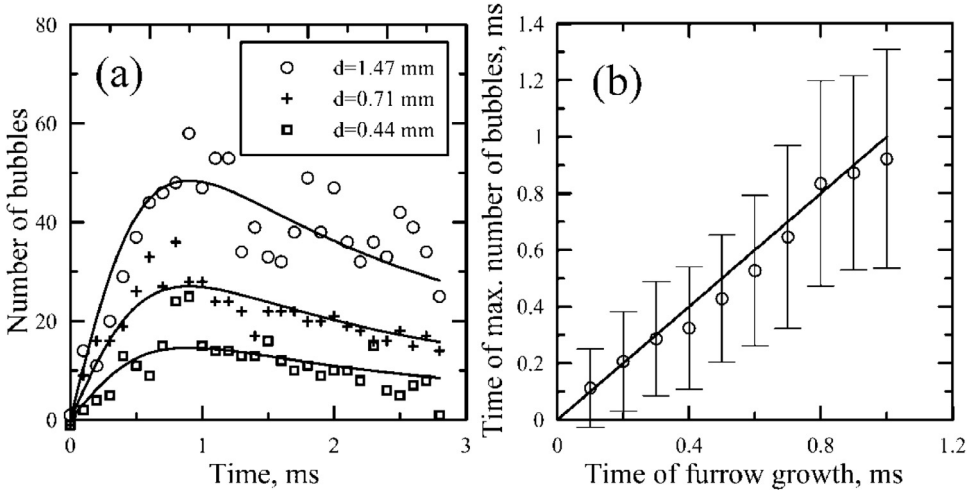

Fig. 15. a) Examples of temporal evolution of the number of bubbles created due to 'furrow' impacts. b) Time of maximum number of bubbles *vs* time of furrow growth.

Thus, V will be always larger than V_{xy} and it also would not work as a criterion of splash. We should note that this criterion also did not work with the data of Okawa et al. (2008) for angles to liquid surface below 30°

Possible alternative is to construct the K number based on vertical velocity V_z. In our case V_z should not reach large values. The contribution of gravity into V_z is limited to 0.7 m/s (the case when a droplet falls from the ceiling of the duct to its bottom). The other possible sources contributing to V_z are related to action of vor-

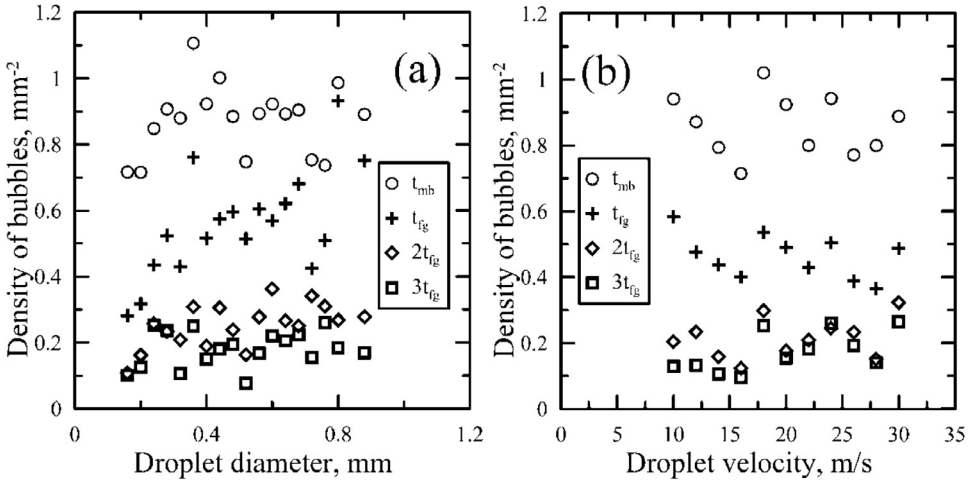

Fig. 16. Average number of bubbles, normalised by the area occupied by furrow, depending on diameter (a) or velocity (b) of impacting droplet at certain time moments. Maximum density of bubbles (1); $t = t_{fg}$ (2); $t = 2t_{fg}$ (3); $t = 3t_{fg}$ (4).

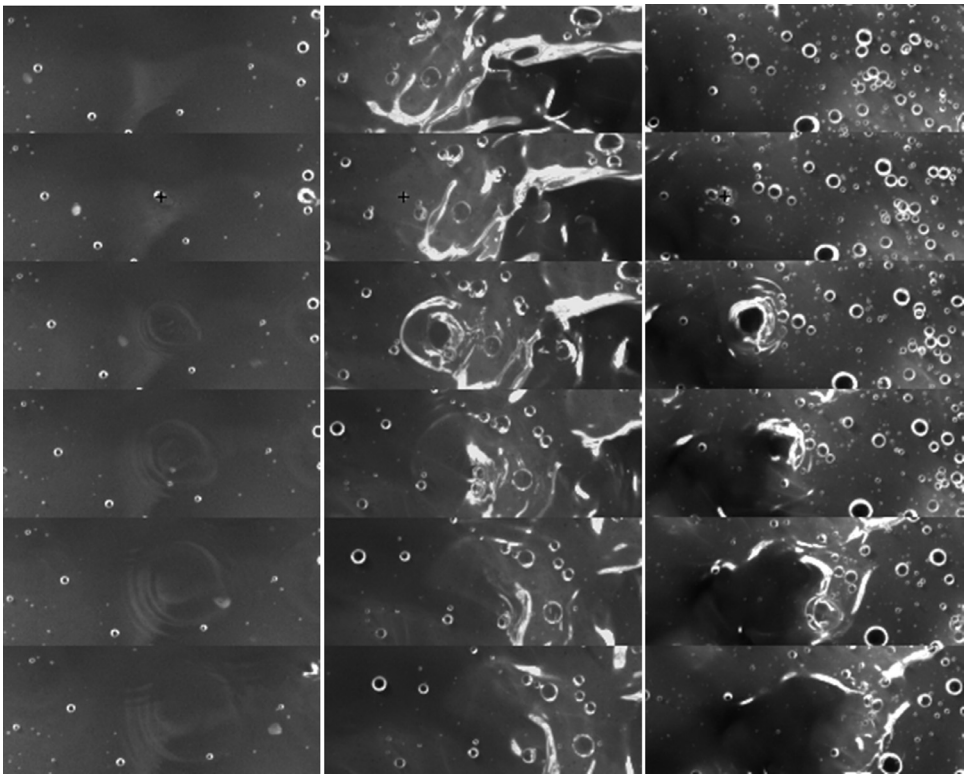

Fig. 17. Examples of craters without secondary entrainment. (a) $V_g = 25$ m/s, $Re_L = 360$. $T = 0.2$ ms; size of the images is 8*3.2 mm. $d = 0.15$ mm, $V_{xy} = 13.2$ m/s. (b) $V_g = 25$ m/s, $Re_L = 360$. $T = 0.4$ ms; size of the images is 8*3.2 mm. $d = 0.24$ mm, $V_{xy} = 23.6$ m/s. (c) $V_g = 35$ m/s, $Re_L = 520$. $T = 0.4$ ms; size of the images is 8*3.2 mm. $d = 0.27$ mm, $V_{xy} = 20$ m/s.

tices in the gas phase or to transverse components of local gas flow (e.g. when gas stream is flowing around a disturbance wave). But these contributions are also expected to be small since the droplet undergoes influence of the vortices during short time and it is known from the work of James et al. (1980) that large enough droplets are not susceptible to the action of turbulent pulsations in the gas phase. Anyway, reaching the value of $K = 2100$ requires $V_z = 14$ m/s for a droplet with diameter of 0.4 mm. Reaching such vertical velocity over the length of 25 mm would require acceleration of 4000 m/s^2, which does not seem realistic.

To conclude, K number based neither on absolute nor on vertical velocity of droplets does not work as criterion for creation of secondary droplets on gas-sheared films. Obviously, the situation with the fast droplet naturally depositing from the gas core onto gas-sheared liquid film is much more complex than that with relatively slow droplets impacting onto static film surface. Besides, K number model works for deep liquid layer and does not take into account the finite depth of gas-sheared liquid films. In addition, effect of local slope or curvature of liquid surface might either enhance or dampen secondary entrainment.

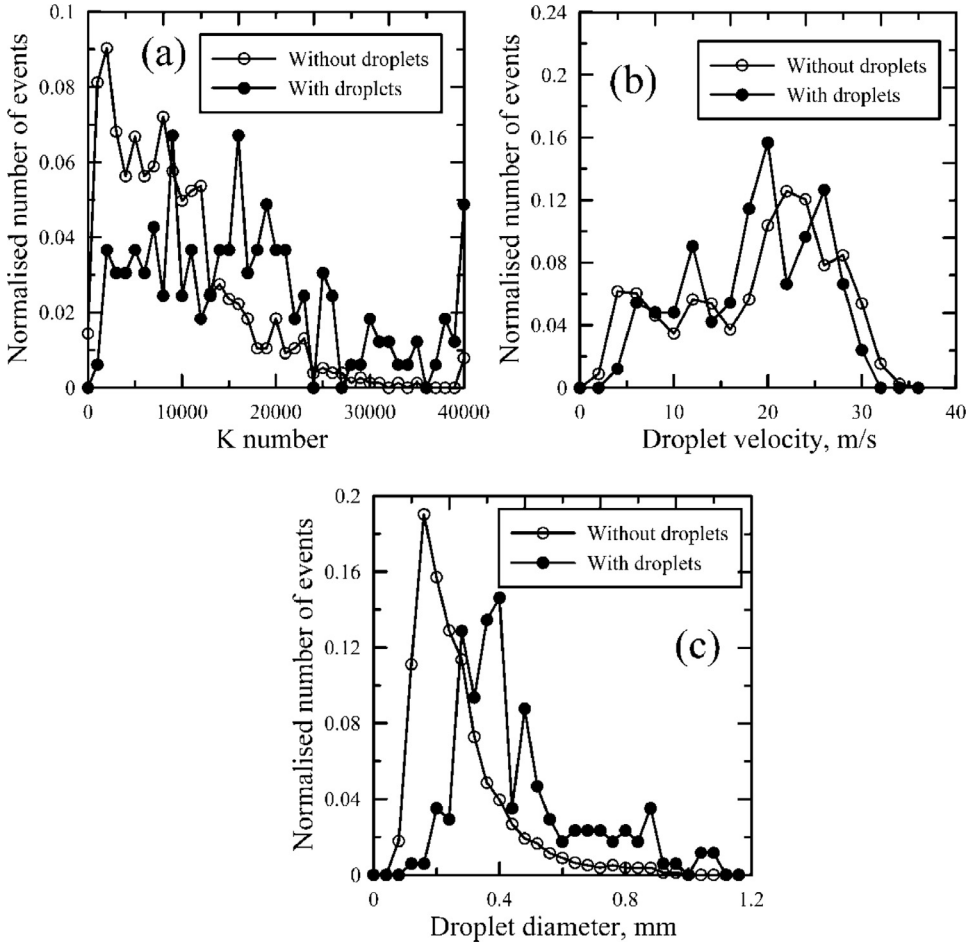

Fig. 18. Comparison of normalized distributions of crater impacts with and without secondary droplets by *K* number (a), horizontal velocity (b) and diameter (c) of impacting droplet.

3.5. Survival of impacting droplet

In about 5% of impact events partial or even complete survival of impacting droplet was observed. Such event was observed by Alekseenko et al. (2014a) during investigation of droplet trajectories in one longitudinal section of the duct: it was found that in such cases the spatiotemporal trajectory of the droplet is continued after interaction with the film without change in velocity; see Fig. 9 (bottom right) in that paper. Both droplet and film are deformed during the interaction. At the initial point of contact either crater or furrow – the latter is much rarer – is created. Deformation of the droplet is rather complex. Below several scenarios of droplet deformation are considered.

In case 1, the whole droplet survives after interaction with liquid film (Fig. 19a). From the point of contact a capillary wave spreads over film surface, either in circular manner or sideways if the area of contact is long enough. The droplet itself is also affected by the interaction: its aspect ratio undergoes temporal variation due to oscillations induced by the interaction. It should also be noted that this scenario is realised at relatively low velocities of impacting droplets, of order of 6 m/s or less.

In case 2 the major part of droplet continues its flight after the contact, but for a while the droplet remains connected to the point of contact by a thin liquid filament (Fig. 19b). As the droplet moves on, the filament is stretched and finally broken into tiny droplets. Description of the mechanisms of a ligament rupture can be found, e.g., in Dumochel et al. (2015), see Figs. 3 and 6 in that paper. The film surface in this case is perturbed much stronger with formation of either a crater or a furrow.

In case 3 a liquid sheet is formed between the area of contact and the survived droplet (see Fig. 20 and also Fig. 7). Due to action of liquid sheet, the droplet is deformed into an arrowhead shape. While the sheet is being stretched, tiny jets are formed on its edges (see also Fig. 2 in Dumouchel et al. 2015). Finally, the jets and the remaining part of liquid sheet are broken into droplets. Surviving part of impacting droplet in this case carries much less liquid than the original droplet did.

It is most likely that which particular scenario occurs is defined by the degree of embedding of the impacting droplet into the liquid film. In case 1 the droplet only slightly touches the film surface without adhering to it. It is even possible that there is no real contact between the film and the droplet in this case due to presence of very thin air layer between them. In the other two cases the bottom of a droplet adheres to film surface, embedding into it to some depth and making either a crater or a furrow. Meanwhile, the top part of the droplet continues its travel. As a result, the middle part of the droplet is stretched between the point of contact and the top part of the droplet. The shape into which the middle part is deformed depends on depth of embedding.

As it can be seen from Figs. 7, 19 and 20, survival event takes place when the contact point is located at a crest of a ripple. Quite obviously, vertical component of droplet's velocity is small in such a case. If such a droplet did not impact onto the crest of a ripple, material of the top part of the droplet would be spread over the base film surface, making a furrow. But, since the point of contact

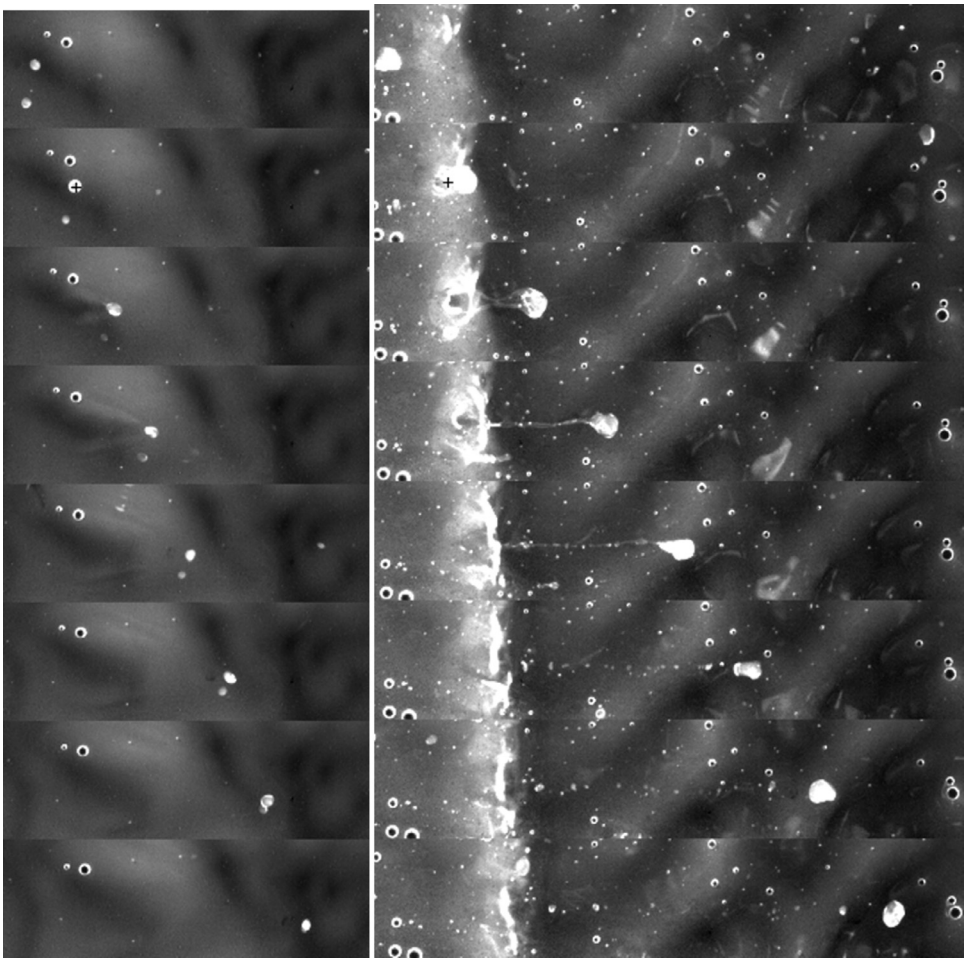

Fig. 19. Examples of survival of impacting droplet. (a) Total survival. $V_g = 30$ m/s, $Re_L = 220$. $T = 0.2$ ms; size of the images is 10*3.2 mm. $d = 0.39$ mm, $V_{xy} = 5.6$ m/s. (b) Partial survival with formation of a liquid filament. $V_g = 30$ m/s, $Re_L = 360$. $T = 0.2$ ms; size of the images is 16*3.2 mm. $d = 0.78$ mm, $V_{xy} = 10$ m/s.

is located above the base film thickness level, the top part of the droplet flies in the air and has a chance to last longer. Cousins and Hewitt (1968) mentioned that the depositing droplets *"underwent series of bounces of low trajectory before being finally absorbed into the film"*. The process of impact with droplet survival may indeed look as bouncing in the cine film images.

Other examples of droplet bouncing were described by Che et al. (2015) for slow droplets falling onto 45° inclined film. Nonetheless, in the present work, for the majority of the cases adhesion and deformation of the impacting droplet is clearly seen. The term "bouncing" might be applicable only to the case 1, but this cannot be confirmed in the present experiments.

Survival events have much similarity to the crater events with creation of secondary droplets (or splash). Indeed, in both cases a droplet creates a crater on film surface and it leads to creation of a number of droplets with different size. Thus, the two events can be easily mixed up during the observations. The best criterion for distinction between the two events is that the velocity of the impacting droplet nearly does not change in the survival case. In the case of splash certain amount of time is required for the crater evolution, formation of the rim and rim breaking. In particular, it is very likely that the 'secondary entrainment' events shown in Fig. 7 in Pham et al. (2014) actually demonstrate the survival of the impacting droplet. In both cases the droplet hits crest of a ripple and its top part does not lose velocity despite being connected to the point of contact. Besides, ligament break-up entrainment event shown in Fig. 6(c) in Pham et al. might actually be a survival event of case 2 (Fig. 19b in the present paper). The important difference between the splash and survival events is that in case of splash the secondary droplets are mainly created from the film liquid, whilst in the case of survival they are mostly created from the impacting droplet material. This distinction may be important in some practical applications in which the droplets are different from the film by physical or chemical properties, temperature, etc.

4. Discussion and conclusions

Impacts of droplets, previously entrained from film surface into the gas core and deposited back onto film surface, are studied experimentally using BBLIF-technique. To the best of our knowledge, this is the first systematic study of impact classification, morphology and outcome for the droplets, "naturally" introduced into the gas core and thus for the situation really taking place in annular flow occurring in various industrial equipment. The main differences between the impacts of "natural" droplets in annular flow and the impacts of artificial droplets in model experiments consist in large velocity and small impingement angle of the droplets and in interaction with gas-sheared wavy film covered with both disturbance waves and ripples.

It was shown that the impacts can be classified into two main types based on the manner of film surface perturbation. The two types of perturbation were called 'craters' and 'furrows'. The former looks as a circular crater with possible asymmetric rim ap-

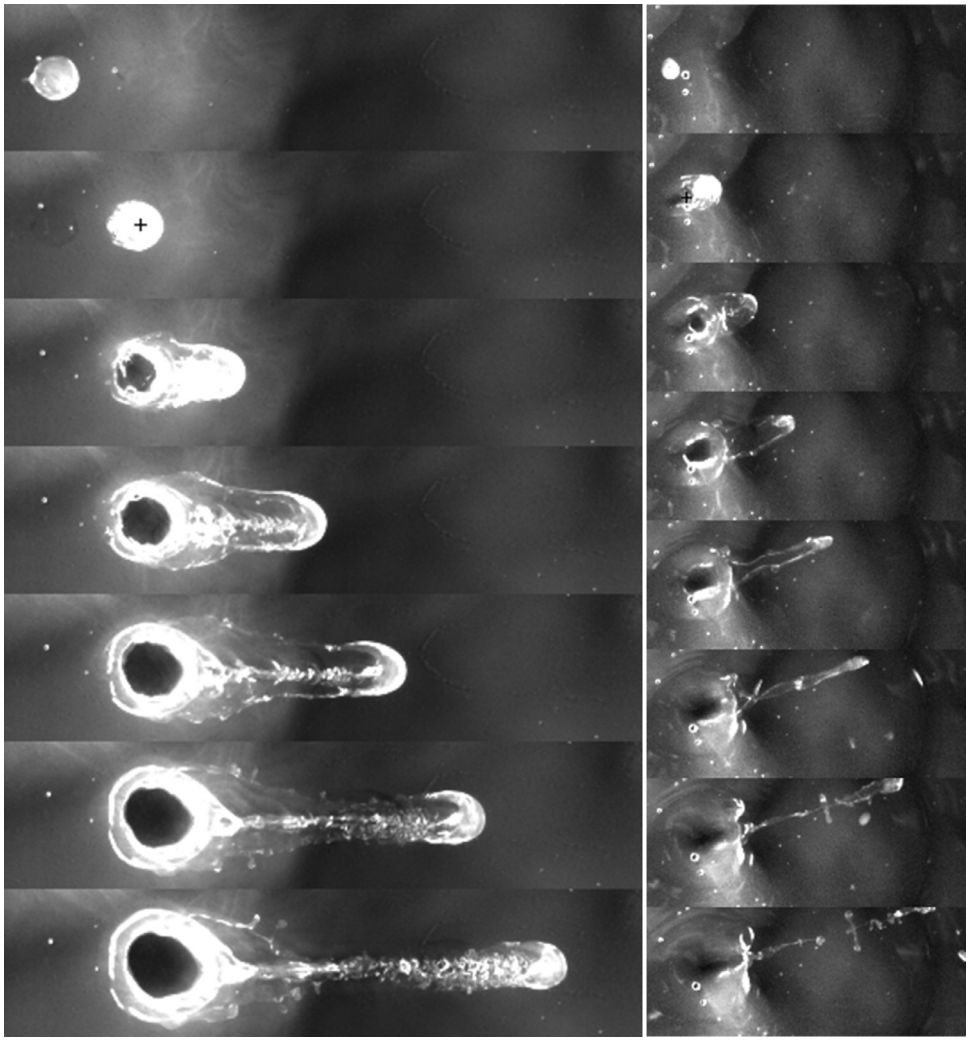

Fig. 20. Rupture of droplet with formation of liquid sheet (a) $V_g = 25$ m/s, $Re_L = 220$. $T = 0.1$ ms; size of the images is 14*3.2 mm. $d = 1.05$ mm, $V_{xy} = 17.6$ m/s. (b) $V_g = 35$ m/s, $Re_L = 360$. $T = 0.1$ ms; size of the images is 8*3.2 mm. $d = 0.61$ mm, $V_{xy} = 9.8$ m/s.

pearing on its leeward side, which is very similar to perturbation of liquid surface by droplets falling under large angles onto still liquid surface. The latter makes long and narrow perturbation covered with transverse wrinkles. Based on comparison to the literature studies of oblique impact onto static film and on indirect evidence from the present measurements, it was assumed that the quantity determining realisation of particular impact type is the angle between the droplet trajectory and the local slope of film surface. From the measurements of film slope and length of furrow the critical angle of impingement for furrow formation was estimated to be about 20°, which is in agreement to the literature data.

Probability of furrow creation due to impact is about twice larger than that of crater creation; this ratio does not change much within the flow conditions range used in the present experiments. Furrows were shown to occur mainly on the base film, whereas craters are much more likely to occur at the disturbance waves. Besides, the total number of impacts increases significantly in front of disturbance waves (due to prompt deposition of newborn droplets) and on the rear slopes of disturbance waves (since these elevations in the film thickness are able to 'catch' the droplets that would otherwise impact farther downstream).

The most important difference between the 'crater' and 'furrow' impacts consists in outcome of the impact. For the crater case, creation of secondary droplets was observed in part of cases (about 15% of all registered crater events). The crater rim in such a case is broken into a number of jets, and each jet is in turn broken into droplets.

The criterion of appearance of secondary entrainment is unclear; the widely used K number does not work here neither being based on absolute velocity of impacting droplet nor on its vertical component.

In contrast to the crater impacts, outcome of the furrow impacts is mainly the bubbles entrapped by the liquid film. The bubbles are created when the droplet protrudes along film surface; after the furrow formation, a portion of the bubbles collapse, but the rest survive and travel inside the film. Number of bubbles created by a furrow is mainly defined by the area of film perturbation, which is in turn mainly defined by the diameter of the impacting droplet.

In about 5% of impact events part of the impacting droplet survived the impact. Such situation occurs when a droplet with small vertical velocity component touches crest of a ripple wave. The middle part of the droplet is strongly deformed while being stretched between the bottom part which had adhered to the film and the top part which continues its flight with its original velocity. The middle part can be deformed into either a liquid filament or liquid sheet depending on depth to which the droplet

embeds into the film. Finally, the middle part is broken into small droplets, whilst the top part of the droplet continues its travel. This event may be considered as a specific case of secondary entrainment in which the secondary droplets are created from the droplet material.

These results are expected to bring some clarification into the available knowledge of droplets deposition in annular gas-liquid flow and to be useful for creation and validation of new models of mass exchange between the gas core and the liquid film. Particular moments that could be taken into account to improve existing models of droplets deposition in annular flow are: non-uniform deposition of droplets in different parts of film surface; influence of the region of deposition on impact type and outcome; probability of secondary entrainment; change of droplet size distribution due to secondary entrainment and survival events; role of droplet impacts in process of bubbles entrapment by liquid film.

Acknowledgements

The work was supported by the UK EPSRC [grant MEMPHIS EP/K003976/1]; Royal Society and Russian Foundation for Basic Research [grant 15-58-10059-KO_a].

Supplementary materials

Supplementary material associated with this article can be found, in the online version, at doi:10.1016/j.ijmultiphaseflow.2016.09.015.

References

Akhmetbekov, Y.K., Alekseenko, S.V., Dulin, V.M., Markovich, D.M., Pervunin, K.S., 2010. Planar fluorescence for round bubble imaging and its application for the study of an axisymmetric two-phase jet. Exp. Fluids 48, 615–629.
Alekseenko, S.V, Cherdantsev, A.V., Heinz, O.M., Kharlamov, S.M., Markovich, D.M., 2014b. Analysis of spatial and temporal evolution of disturbance waves and ripples in annular gas–liquid flow. Int. J. Multiphase Flow 67, 122–134.
Alekseenko, S.V., Antipin, V.A., Cherdantsev, A.V., Kharlamov, S.M., Markovich, D.M., 2008. Investigation of waves interaction in annular gas-liquid flow using high-speed fluorescent visualization technique. Microgravity Sci. Technol. 20, 271–275.
Alekseenko, S.V., Cherdantsev, A.V., Markovich, D.M., Rabusov, A.V., 2014a. Investigation of droplets entrainment and deposition in annular flow using LIF technique. Atomization Sprays 24, 193–222.
Alghoul, S., Eastwick, C., Hann, D., 2011. Droplet impact on shear-driven liquid films. Atomization Sprays 21, 833–846.
Azzopardi, B.J., 1983. Mechanisms of Entrainment in Annular Two-Phase Flow. UKAEA Report AERE-R 11068.
Azzopardi, B.J., 1987. Observations of drop motion in horizontal annular flow. Chem. Eng. Sci. 42 (8), 2059–2062.
Azzopardi, B.J., 1997. Drops in annular two-phase flow. Int. J. Multiphase Flow 23, 1–53.
Azzopardi, B.J., Teixeira, J.C.F., 1994. Detailed measurements of vertical annular two-phase flow—part I: drop velocities and sizes. J. Fluids Eng. 116 (4), 792–795.
Azzopardi, B.J., Zaidi, S.H., 1998. Drop sizes and velocities in annular two-phase flow. 14th Annual Conference on Liquid Atomisation and Spray Systems, Manchester, U.K., July 6-8, 1998.
Badie, S., 2000. Horizontal Stratifying/Annular Gas-Liquid Flow Ph.D. thesis. Imperial College, London.
Bisighini, A., Cossali, G.E., Tropea, C., Roisman, I.V., 2010. Crater evolution after the impact of a drop onto a semi-infinite liquid target. Phys. Rev. E - Statist. Nonlinear Soft Matter Phys. 82.
Che, Z., Deygas, A., Matar, O.K., 2015. Impact of droplets on inclined flowing liquid films. Phys. Rev. E 92, 023032.
Cherdantsev, A.V., Hann, D.B., Azzopardi, B.J., 2014. Study of gas-sheared liquid film in horizontal rectangular duct using high-speed LIF technique: three-dimensional wavy structure and its relation to liquid entrainment. Int. J. Multiphase Flow 67, 52–64.
Cioncolini, A., Thome, J.R., 2010. Prediction of the entrained liquid fraction in vertical annular gas–liquid two-phase flow. Int. J. Multiphase Flow 36, 293–302.
Cousins, L.B., Hewitt, G.F., 1968. Liquid Phase Mass Transfer in Annular Two-Phase Flow: Droplet Deposition and Liquid Entrainment. UKAEA report AERE - R 5657.
Dumouchel, C., Blaisot, J.-B., Bouche, E., Ménard, T., Vu, T.-T., 2015. Multi-scale analysis of atomizing liquid ligaments. Int. J. Multiphase Flow 73, 251–263.
Fore, L.B., Dukler, A.E., 1995. The distribution of drop size and velocity in gas-liquid annular flow. Int. J. Multiphase Flow 21, 137–149.
Hann, D.B., Cherdantsev, A.V., Mitchell, A., McCarthy, I.N., Hewakandamby, B.N., Simmons, K., 2016. A study of droplet impact on static films using the BB-LIF technique. Exp. Fluids 57 (4), 1–12.
James, P.W., Hewitt, G.F., Whalley, P.B., 1980. Droplet motion in two-phase flow. In: ANS/ASME Topical Meeting on Reactor Thermal-Hydraulics; Saratoga, NY, USA; 9 - 12 Oct 1980, pp. 1484–1503.
Lagubeau, G., Fontelos, M.A., Josserand, C., Maurel, A., Pagneux, V., Petitjeans, P., 2012. Spreading dynamics of drop impacts. J. Fluid Mech. 713, 50–60.
Leman, G.W., Agostini, M., Andreussi, P., 1985. Tracer analysis of developing two-phase annular flow. PCH Phys. Chem. Hydrodyn. 6 (1/2), 223–237.
Leneweit, G., Koehler, R., Roesner, K.G., Schaffer, G., 2005. Regimes of drop morphology in oblique impact on deep fluids. J. Fluid Mech 543, 303–331.
Oguz, H.N., Prosperetti, A., 1990. Bubble entrainment by the impact of drops on liquid surfaces. J. Fluid Mech. 219, 143–179.
Okawa, T., Shiraishi, T., Mori, T., 2008. Effect of impingement angle on the outcome of single water drop impact onto a plane water surface. Exp. Fluids 44, 331–339.
Pan, L., Hanratty, T.J., 2002. Correlation of entrainment for annular flow in vertical pipes. Int. J. Multiphase Flow 28, 363–384.
Pham, S.H., Kawara, Z., Yokomine, T., Kunugi, T., 2014. Detailed observations of wavy interface behaviors of annular two-phase flow on rod bundle geometry. Int. J. Multiphase Flow 59, 135–144.
Pitton, E., Ciandri, P., Margarone, M., Andreussi, P., 2014. An experimental study of stratified–dispersed flow in horizontal pipes. Int. J. Multiphase Flow 67, 92–103.
Samenfink, W., Elsäßer, A., Dullenkopf, K., Wittig, C., 1999. Droplet interaction with shear-driven liquid films: analysis of deposition and secondary droplet characteristics. Int. J. Heat Fluid Flow 20 (5), 462–469.
Sawant, P., Ishii, M., Mori, M., 2008. Droplet entrainment correlation in vertical upward co-current annular two-phase flow. Nucl. Eng. Des. 238, 1342–1352.
Thoroddsen, S.T., Etoh, T.G., Takehara, K., 2003. Air entrainment under an impacting drop. J. Fluid Mech. 478, 125–134.
Thoroddsen, S.T., Etoh, T.G., Takehara, K., 2008. High-speed imaging of drops and bubbles. Ann. Rev. Fluid Mech. 40, 257–285.
Van Hinsberg, N.P., Budakli, M., Gohler, S., Berberovich, E., Roisman, I.V., Gambaryan-Roisman, T., Tropea, C., Stephan, P., 2010. Dynamics of the cavity and the surface film for impingements of single drops on liquid films of various thicknesses. J. Coll. Interface Sci. 350, 336–343.
Watanabe, Y., Saruwatari, A., Ingram, D.M., 2008. Free-surface flows under impacting droplets. J. Comp. Phys. 227, 2344–2365.
Woodmansee, D.E., Hanratty, T.J., 1969. Mechanism for the removal of droplets from a liquid surface by a parallel air flow. Chem. Eng. Sci. 24, 299–307.
Worthington, A.M., 1877. On drops. Nature 16, 165–166.
Zhao, H., Ecault, R., Dorao, C.A., Munkejord, S.T., 2011. Splashing of water droplets on a tilted flowing liquid film. DIPSI Workshop on Droplet Impact Phenomena & Spray Investigation. May 27, 2011. Bergamo, Italy.